

THE PROPERTIES OF THE CIRCUMGALACTIC MEDIUM IN RED AND BLUE GALAXIES: RESULTS FROM THE COS-GASS+COS-HALOS SURVEYS

SANCHAYEETA BORTHAKUR

Department of Physics & Astronomy, Johns Hopkins University, Baltimore, MD, 21218, USA; The Astronomy Department, University of California, Berkeley, CA, USA

TIMOTHY HECKMAN

Department of Physics & Astronomy, Johns Hopkins University, Baltimore, MD, 21218, USA

JASON TUMLINSON

Space Telescope Science Institute, Baltimore, MD, USA

RONGMON BORDOLOI

MIT-Kavli Center for Astrophysics and Space Research, Cambridge, MA, USA

GUINEVERE KAUFFMANN

Max-Planck Institut für Astrophysik, D-85741 Garching, Germany

BARBARA CATINELLA

International Centre for Radio Astronomy Research, The University of Western Australia, 35 Stirling Highway, Crawley WA 6009, Australia

DAVID SCHIMINOVICH

Department of Astronomy, Columbia University

ROMEEL DAVÉ

University of the Western Cape, Bellville, Cape Town 7535,
South Africa, South African Astronomical Observatories, Observatory, Cape Town 7925,
South Africa, African Institute for Mathematical Sciences, Muizenberg, Cape Town 7945, South Africa

SEAN M. MORAN

Harvard-Smithsonian Center for Astrophysics, 60 Garden Street, Cambridge, MA 02138

AMELIE SAINTONGE

Department of Physics and Astronomy, University College London, Gower Place, London WC1E 6BT, UK

Accepted for publication in ApJ: Sep 20, 2016

ABSTRACT

We use the combined data from the COS-GASS and COS-Halos surveys to characterize the Circum-Galactic Medium (CGM) surrounding typical low-redshift galaxies in the mass range $M_* \sim 10^{9.5-11.5} M_\odot$, and over a range of impact parameters extending to just beyond the halo virial radius (R_{vir}). We find the radial scale length of the distributions of the equivalent widths of the Lyman α and Si III absorbers to be 0.9 and 0.4 R_{vir} , respectively. The radial distribution of equivalent widths is relatively uniform for the blue galaxies, but highly patchy (low covering fraction) for the red galaxies. We also find that the Lyman α and Si III equivalent widths show significant positive correlations with the specific star-formation rate (sSFR) of the galaxy. We find a surprising lack of correlations between the halo mass (virial velocity) and either the velocity dispersions or velocity offsets of the Lyman α lines. The ratio of the velocity offset to the velocity dispersion for the Lyman α absorbers has a mean value of ~ 4 , suggesting that a given the line-of-sight is intersecting a dynamically coherent structure in the CGM rather than a sea of orbiting clouds. The kinematic properties of the CGM are similar in the blue and red galaxies, although we find that a significantly larger fraction of the blue galaxies have large Lyman α velocity offsets ($> 200 \text{ km s}^{-1}$). We show that - if the CGM clouds represent future fuel for star-formation - our new results could imply a large drop in the specific star-formation rate across the galaxy mass-range we probe.

Subject headings: galaxies: halos — galaxies: starbursts — galaxies: ISM — quasars: absorption lines

1. INTRODUCTION

Galaxy growth is fundamentally connected to the cycle of accretion and ejection of matter into and out of galaxies. In the simplest picture, galaxies acquire gas that reaches the central regions via the circum-galactic medium (CGM). There it condenses into neutral and then molecular gas, some of which is then converted into stars. Young stars in turn drive strong winds, outflows, and radiation that deposit mass, metals, energy, and momentum to the CGM, thus significantly influencing its properties (see review by Somerville & Davé 2015; Fielding et al. 2016, and references therein). These linked processes are commonly termed the baryon cycle. The CGM then lies at the heart of this cycle, as it is the interface between the stellar body of the galaxy and the intergalactic medium. It is the primary spatial pathway for the baryon cycle into and out of galaxies (Ford et al. 2016; Tumlinson et al. 2013; Borthakur et al. 2015; Nielsen et al. 2015; Shen et al. 2014; Mitra et al. 2015; Brook et al. 2014, and references therein).

The CGM is also a reservoir of low-density gas that may have as much mass as the stellar component of the galaxy (Werk et al. 2013, 2014; Tumlinson et al. 2013; Peebles et al. 2014; Richter et al. 2016). It extends out from the stellar disk out to the virial radius of the galaxy (Chen et al. 2001a; Stocke et al. 2013; Borthakur et al. 2013). However, due to its low surface-brightness, we have not yet been able to directly image this vast baryonic reservoir. On the other hand, absorption-line spectroscopy provides an avenue to probe the physical conditions in this low-density gaseous medium. Rest-frame ultra-violet (UV) spectroscopy enables us to use various absorption-line transitions, including hydrogen and metal-line species spanning a broad range of ionization states.

Mapping the CGM with the help of a large sample of sightlines probing a range of impact parameters is crucial for understanding its properties and its variations as a function of radius. The radial dependence in the properties of the neutral hydrogen in the CGM has been known for decades, based on observations of the Lyman α absorption-line (Lanzetta et al. 1995; Chen et al. 1998; Tripp et al. 1998; Chen et al. 2001b; Bowen et al. 2002; Prochaska et al. 2011; Stocke et al. 2013; Tumlinson et al. 2013; Liang & Chen 2014; Borthakur et al. 2015, and references therein). However, only recently, with the installation of Cosmic Origins Spectrograph (COS) aboard the Hubble Space Telescope (HST), has it become feasible to undertake detailed probes of the CGM properties as a function of other global properties of the central galaxy.

One of the consequences of the accretion of gas passing through the CGM is that this provides the raw material to sustain the growth of the galaxy via star formation (e.g. Bouché et al. 2013). Not all galaxies produce stars at the same rate (Brinchmann et al. 2004a; Salim et al. 2007; Noeske et al. 2007; Daddi et al. 2007;

Rodighiero et al. 2011; Speagle et al. 2014; Snyder et al. 2015). In particular, galaxies show two distinct populations in terms of their star-formation rate (SFR). While most low mass galaxies form stars at significant rates, most high mass galaxies produce stars at negligible levels. This was termed as the galaxy color bimodality defined in terms of “blue” (star-forming) galaxies and “red” (quiescent) galaxies (e.g. Kauffmann et al. 2003; Blanton et al. 2003; Baldry et al. 2004; Brinchmann et al. 2004b; Tully et al. 1982).

About a decade back, cosmological hydrodynamical simulations revealed two distinct ways that galaxies accrete gas into their dark matter halo as a function of halo mass. The predominant mode of gas accretion for low mass galaxies is believed to be the “cold” mode (Kereš et al. 2005, 2009; Dekel et al. 2009), where gas falls into galaxies as streams or lumps at temperatures much less than that of the virial temperature. For the higher mass halos, the accretion process is expected to be in the “hot” mode (White & Frenk 1991; Fukugita & Peebles 2006), in which the incoming gas shock heats to the virial temperature. This broadly can explain why high-mass galaxies have little to no cold gas reservoirs to fuel star-formation (see work on condensation in hydrodynamical simulations by Kaufmann et al. 2006, 2009; Sommer-Larsen 2006). Galaxies also recycle gas from previous generations of star-formation that is stored in their CGM (Ford et al. 2013; Fraternali et al. 2015). However, the process of how gas gets into the disk from the CGM is fairly complex. Nonlinear perturbations in the filamentary flows may help the cool accreting gas condense and add cold gas to the disk (Kereš & Hernquist 2009; Joung et al. 2012a). These condensing clouds may contain as much as 25%-75% of the cold gas in the CGM (Fernández et al. 2012).

In addition to accretion, star-formation driven feedback may change the nature and properties of the gas in the CGM (Kauffmann et al. 2016; Liang et al. 2016; Nelson et al. 2015, 2016; Marasco et al. 2015). Massive young stars inject energy and/or momentum into outflows (Veilleux et al. 2005; Heckman et al. 2011; Borthakur et al. 2014; Heckman et al. 2015; Heckman & Borthakur 2016) that may travel into the CGM, enriching it with metals, shock-heating the cooler CGM clouds, and possibly even expelling/unbinding the CGM (Borthakur et al. 2013). Therefore, if feedback provided by massive stars plays a role in the observed bimodality, then we should see a change in the structure, ionization state, and/or kinematics of the CGM as a function of SFR.

To that end, we have selected a subsample of galaxies from the GALEX Arecibo SDSS Survey (GASS; Catinella et al. 2010, 2012, 2013) that have background UV-bright quasi-stellar objects (QSOs) located within a projected distance of 250 kpc in the rest-frame of the galaxy. This yielded the COS-GASS sample (Borthakur et al. 2015) whose members were observed with COS using the G130M grating. This provided a spectral $R=20,000-24,000$ (FWHM ~ 12 to 15 km s $^{-1}$). We have multi-band data for these galaxies from

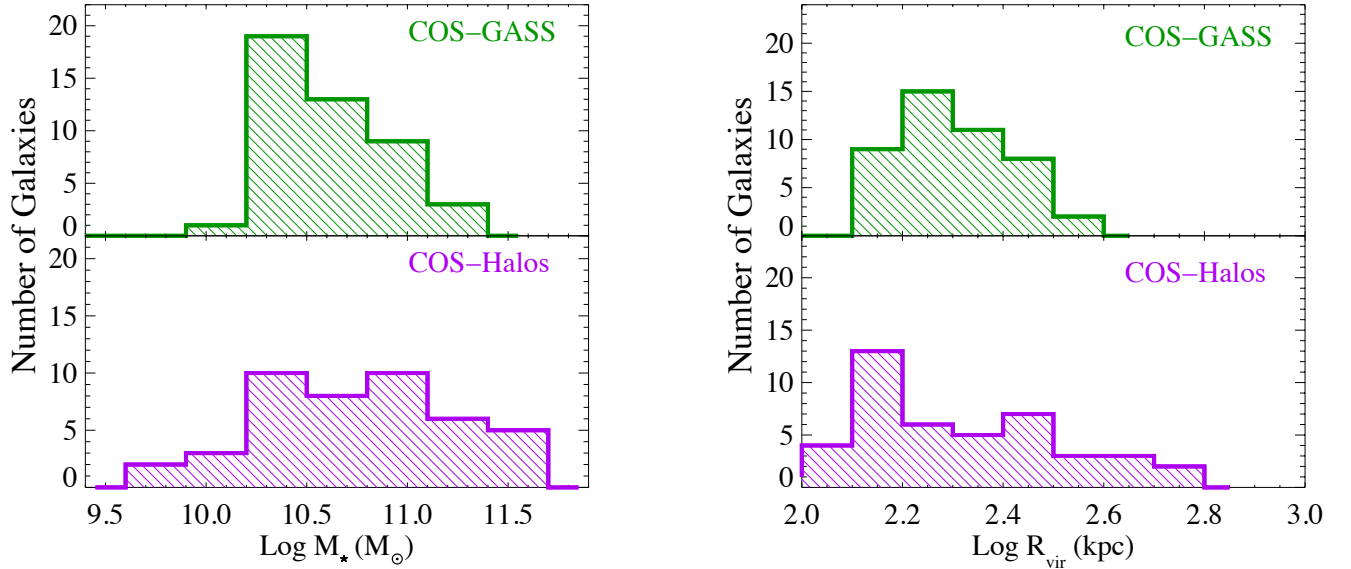


FIG. 1.— Distribution of galaxy properties for the COS-GASS and COS-Halos samples. The left panel shows the stellar mass distribution and the right panel shows the virial radius distribution. The R_{vir} for both the samples were estimated using the prescription described by Kravtsov et al. (2014); Mandelbaum et al. (2016); Liang & Chen (2014) as described in section 2.1.

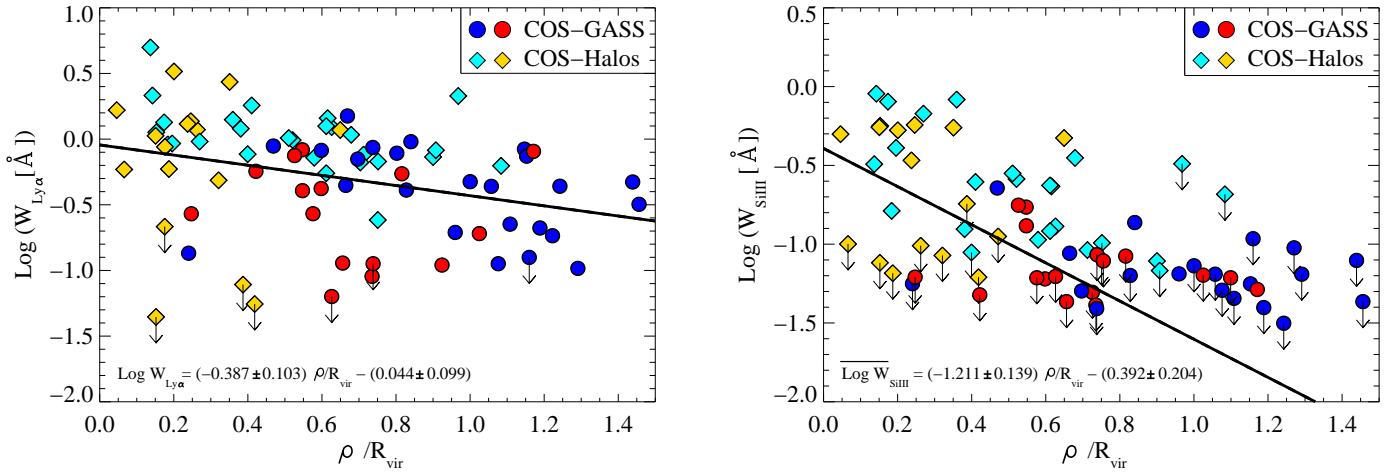


FIG. 2.— Variation of Lyman α and Si III equivalent width with normalized impact parameter (i.e. ρ/R_{vir}) for a combined COS-GASS and COS-Halos sample. The colors blue and cyan indicate “blue” galaxies and red and yellow denote “red” galaxies. The black thick line denotes the fits to the data using the Buckley-James method. The calculations were performed using the survival analysis software ASURV that takes into account the censored data. The parameters describing the best-fit lines are printed at the bottom left corner. Since the fits presented here take into account the censored data, the parameters of the best-fit in the left panel are slightly different from those published by Borthakur et al. (2015).

the parent GASS survey: 21 cm H I spectroscopic data obtained with the Arecibo telescope, optical images and spectroscopy from the Sloan Digital Sky Survey (SDSS), UV imaging with the Galaxy Evolution Explorer (GALEX), molecular gas data from IRAM (COLD GASS; Saintonge et al. 2011), and long-slit optical spectroscopy (Moran et al. 2012) for a portion of the sample. Therefore, we have the stellar mass, SFR, gas-phase metallicity, stellar morphology, and atomic and molecular gas masses for all the 45 galaxies from the COS-GASS sample.

Here we present our study utilizing the combined COS-GASS (Borthakur et al. 2015) and COS-Halos (Tumlinson et al. 2013) samples. Detailed descriptions of our sample, the COS observations and data reduction are presented in Section 2. The results are presented in Section 3 and their implications are discussed in Section 4. Finally, we summarize our findings in Section 5. The cosmological parameters used in this study are $H_0 = 70 \text{ km s}^{-1} \text{ Mpc}^{-1}$ (in between the two recent measurements of $73.24 \pm 1.74 \text{ km s}^{-1} \text{ Mpc}^{-1}$ (Riess et al. 2016) and $67.6^{+0.7}_{-0.6} \text{ km s}^{-1} \text{ Mpc}^{-1}$ (Grieb et al. 2016)),

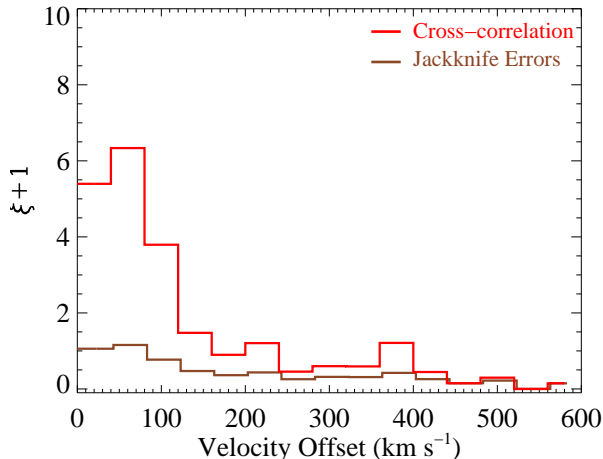


FIG. 3.— The cross-correlation function between the galaxy systemic velocities and velocity centroids of Lyman α absorbers. The cross-correlation function was calculated using the same data analysis criterion as the observations/measurements. For example, the absorbers were randomly distributed within the allowed velocity range of $\pm 600 \text{ km s}^{-1}$. Caution must be applied when comparing these results to those from blind surveys or surveys with different intrinsic resolutions for the spectrograph.

$\Omega_m = 0.3$, and $\Omega_\Lambda = 0.7$. We note that varying the Hubble constant value from 65 to 75 $\text{km s}^{-1} \text{ Mpc}^{-1}$ does not affect the conclusions in the paper.

2. OBSERVATIONS

2.1. Sample

We combined the COS-GASS sample (45 galaxies) with the COS-Halos sample (44 galaxies) to get our full sample. The COS-Halos sightlines cover the inner CGM (thoroughly up to $\sim 0.8R_{\text{vir}}$) whereas the COS-GASS sightlines extend the observations to the outer CGM ($\sim 0.05-1.5R_{\text{vir}}$). The resulting combined sample contains a total of 89 sightlines probing the CGM from 17-231 kpc in the rest frame of the target galaxies.

The two programs probe similar stellar mass ranges. The COS-Halos program probes galaxies in the range $10^{9.6-11.5} M_\odot$ at $0.1 < z < 0.2$ whereas the COS-GASS program probes galaxies in the range ($10^{10.1-11.1} M_\odot$) at slightly lower redshifts of $0.02 < z < 0.05$. A comparison of the stellar masses and virial radii (based on the prescription by Kravtsov et al. (2014) and Liang & Chen (2014)) for both samples are provided in Figure 1. Recent gravitational-lensing-based results by Mandelbaum et al. (2016) show that blue galaxies of fixed stellar mass are found in lower mass halos than red galaxies of the same stellar mass. Based on their results, we add (subtract) 0.15 dex to the halo masses for red (blue) galaxies with a given stellar mass. The dark matter halo masses of the combined sample range from 11.1 to 13.2 M_\odot dex. We note that the redshift difference between the two samples is ~ 0.1 . However, the variation in CGM properties during this time is expected to be minimal (Chen 2012). Also, the COS-Halos sample was selected to be all centrals (with a couple of non-centrals Tumlinson et al. 2013, section 2.5). This is not one of the criteria for COS-GASS, although the mass range of the galaxies ensured that most of the COS-GASS galaxies (34/45) are centrals (based on the group catalog by Yang et al. 2005, 2007). So the combined sample is 85% centrals. We have retained the satellites in our analysis, but have verified

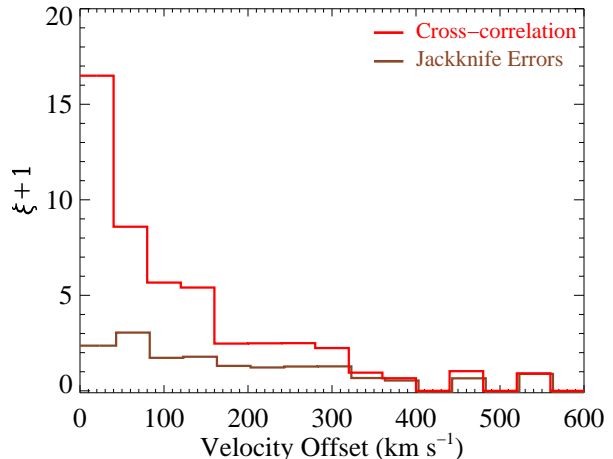


FIG. 4.— The cross-correlation function between velocity centroids of Lyman α and Si III absorbers. The calculations for the cross-correlation function preserved the distribution of the Lyman α absorbers with respect to the galaxy systemic velocity as discussed in Figure 3.

that they do not affect any of our conclusions.

We identify galaxies with specific star formation rates ($\text{sSFR} = \text{SFR}/M_\star > 10^{-11} \text{ yr}^{-1}$) as blue (star-forming) galaxies and those below this limit as red (quiescent) galaxies. sSFR values of $< 10^{-12} \text{ yr}^{-1}$ can be considered as upper limit. A detailed description of our galaxy color assignment can be found in Borthakur et al. (2015).

For more information on the properties of the target galaxies, including their redshifts, stellar masses, SFRs^1 , sSFR , galaxy colors, and impact parameter of the sightlines, we refer the reader to Table 1 presented in this paper (for the COS-GASS sample) and Table 2 from the published work by Tumlinson et al. (2013).

2.2. Observations and Data Reduction

The data presented in this paper were obtained under the COS-GASS survey (program=12603; P.I. Heckman) observed with the COS aboard the HST using the high resolution grating G130M ($R = 20,000-24,000$; $\text{FWHM} = 12-15 \text{ km s}^{-1}$). The wavelength coverage of the spectrograph is 1140-1470 Å. The galaxies being at lower redshift (maximum redshift of 0.05) allows us to probe a wide variety of far-UV line transitions such as Lyman α ($\lambda 1216$), Si II ($\lambda 1190, 1193, \& 1260$), Si III ($\lambda 1206$), Si IV ($\lambda \lambda 1393, 1402$), C II ($\lambda 1334$), and O I ($\lambda 1302$).

Absorption features that have equivalent widths larger than 3 times the noise in the spectra were picked out and then identified both in terms of the transition and redshift. This allowed us to detect any contamination to the absorption associated with the target galaxies. We searched in a velocity window of $\pm 600 \text{ km s}^{-1}$ from the systemic velocity (using optimal redshift from SDSS that is tracing the stars and ionized gas in the central region of the galaxies) for associated absorbers. The absorbers were measured and Voigt profile fits were performed. More information on the data reduction can be found in the previous publication of COS-GASS (Borthakur et al. 2015). This procedure is exactly same as followed by

¹ The SFR for the GASS sample were derived by combining GALEX *FUV* and *NUV* and SDSS *u, g, r, i, z* photometry and SDSS spectral-line indices.

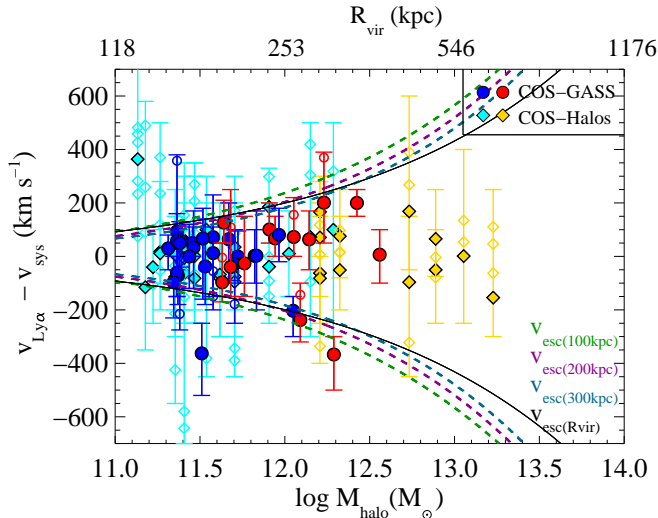


FIG. 5.— Velocity distribution of Lyman α transitions with respect to the systemic velocity of the host galaxies for the COS-GASS and COS-Halos samples. The color of the symbols show the color of the galaxy (blue and cyan for “blue” galaxies and red and yellow for “red” galaxies) and the vertical colored bar shows the extent of absorption. The centroids of the strongest component are shown as the filled symbols and the weaker components are shown as open symbols. The escape velocity required for the gas clouds to escape the halos at impact parameters of 100, 200, and 300 kpc are shown as colored dashed curves and that at the virial radius as solid black curve. The velocity distribution of metal species is very similar to this plot, although the constraints are weaker due to multiple non-detections.

Tumlinson et al. (2013); Werk et al. (2013) for the COS-Halos program.

3. RESULTS

The COS-GASS survey covered a wavelength range of $\approx 1150\text{--}1450\text{\AA}$ for most galaxies. This includes the prominent transitions like H I Lyman α $\lambda 1216$, O I $\lambda 1302$, C II $\lambda 1334$, Si II $\lambda 1260, 1193, 1190$, Si III $\lambda 1206$, Si IV $\lambda\lambda 1393, 1402$, and N V $\lambda 1239$. H I Lyman α and Si III $\lambda 1206$ are the strongest lines detected in our sample. In this paper, we will primarily focus on these two most sensitive probes. A paper presenting all the other metal-lines detected in COS-GASS survey is in preparation. Table 2 presents the measurements for Lyman α and Si III for each of the sightlines from the COS-GASS sample. In cases where we do not detect any absorption features, we quote a 3σ equivalent width as the upper limit. The detection limits for the COS-GASS sample are typically ~ 50 mÅ, which corresponds to $\text{Log } N(\text{H I}) = 12.96$, $\text{Log } N(\text{Si II}) = 12.55$, $\text{Log } N(\text{Si III}) = 12.37$, $\text{Log } N(\text{Si IV}) = 13.05$, and $\text{Log } N(\text{C II}) = 13.39$, respectively.

The measurements for COS-Halos sightlines can be found in the published work by Werk et al. (2013).

3.1. Overall Detection Rates

The Lyman α absorption-line, produced by neutral Hydrogen, is the strongest transition found in the combined data. Lyman α absorption was detected in 75/82 ($91_{-15}^{+9}\%$) sightlines where measurements could be made. This detection rate is consistent with those found by Prochaska et al. (2011); Stocke et al. (2013); Liang & Chen (2014). Often the absorption features are

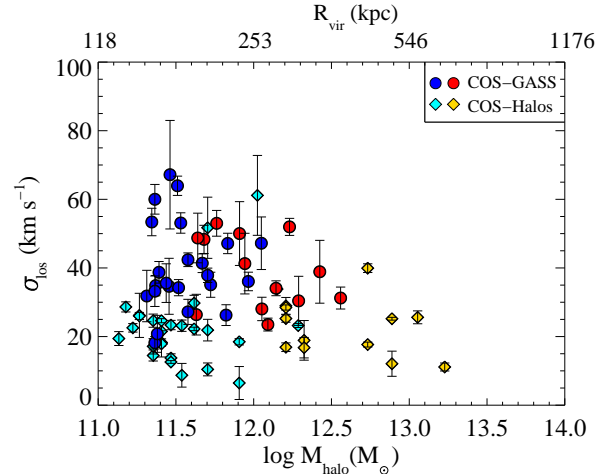


FIG. 6.— The line-of-sight velocity dispersion for the strongest component of the Lyman α absorption line plotted as a function of the halo mass. There is no significant correlation between these parameters.

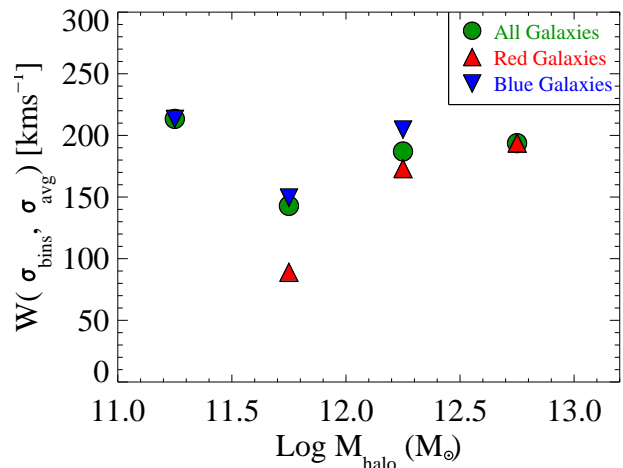


FIG. 7.— Velocity parameter, W , as a function of halo mass. The parameter W defined as $W^2 = \sigma_{\text{bin}}^2 + \sigma_{\text{avg}}^2$ where σ_{bin} is the dispersion of the centroids within each bin and the σ_{avg} is the average velocity dispersion (width) among the absorption features within the bins. The full sample is shown in green and the red and blue galaxies are shown as red and blue triangles. The value of W does not change significantly between halo masses of $10^{11\text{--}13} M_{\odot}$ for the entire sample.

saturated and hence we use the equivalent width for our analysis, as we are not able to accurately determine the column densities of these absorbers. The Lyman α is primarily tracing $\approx 10^{4\text{--}5.5}$ K (based on the Doppler widths²).

The Si III $\lambda 1206.5$ absorption-line is the strongest feature tracing metals in the COS-GASS survey, thus making it the most sensitive tracer of the warm CGM (also see Collins et al. 2009; Shull et al. 2009; Lehner et al. 2012, 2015; Richter et al. 2016). Out of 37 sightlines for the COS-GASS sample, where data were uncontam-

² This does not rule out a the presence of a substantial “hot” medium at temperatures of $\approx T > 10^6$ K that may be traced by species like O VII

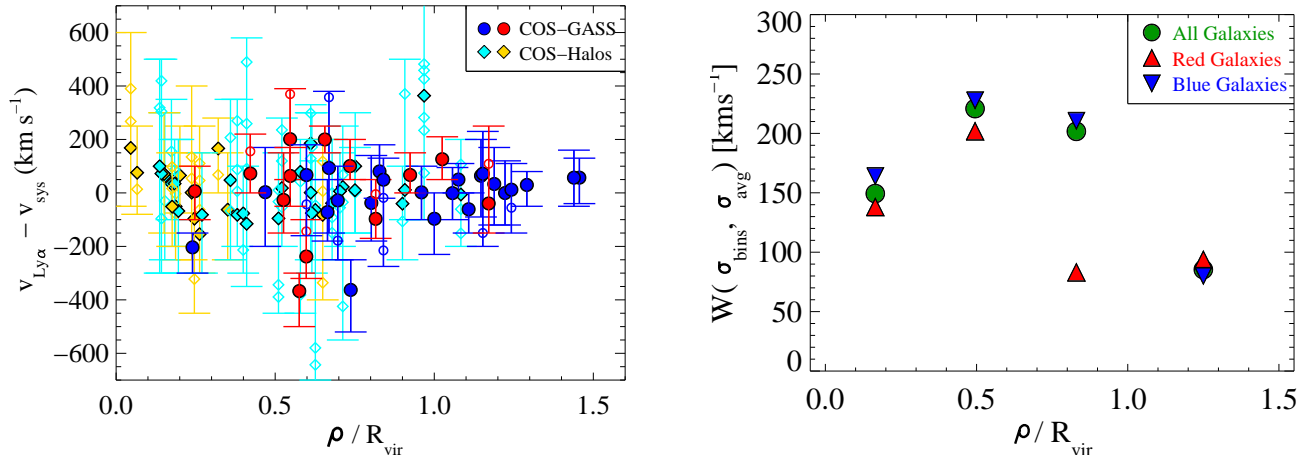


FIG. 8.— Velocity distribution of Lyman α transitions with respect to the systemic velocity of the host galaxies as a function of normalized impact parameter (ρ/R_{vir}) for the COS-GASS and COS-Halos samples. The circles represent the COS-GASS sample and the diamonds represent the COS-Halos sample. The color of the symbols indicate the color of the galaxy i.e. blue and cyan for “blue” galaxies and red and yellow for “red” galaxies.

inated and measurements could be made, we detected Si III in 11 of them. Thus the detection rate of Si III in the outer halo is $30 \pm 10\%$. This is smaller than results for the inner CGM, as found by Werk et al. (COS-Halos survey; 2013), Liang & Chen (2014) and Richter et al. (2016)³. Since our study primarily focuses on the outer CGM ($0.5R_{\text{vir}} < \rho < 1.5R_{\text{vir}}$ with the exception of two inner sightlines), a more relevant comparison would be the covering fraction of Si III of $14_{-5}^{+11}\%$ for sightlines with $0.54 R_{\text{vir}} < \rho < 1.02 R_{\text{vir}}$ by Liang & Chen (2014). Both the numbers are broadly consistent given that the error ranges in the estimate do have an overlap. Interesting, the two inner sightlines in the COS-GASS sample, which one might naively think are contributing the excess in our detection rate are devoid of any Si III absorption. However, in the broad context of metals in the outer CGM, our study find consistently lower metal covering fraction thus suggesting that metals are rarer in the outer CGM similar to conclusions of Liang & Chen (2014) and Bordoloi et al. (2014, for C IV from the COS-Dwarfs survey). The combined sample has a detection rate of Si III of $49 \pm 10\%$.

The detection rate of C II, Si II and Si IV in the COS-GASS sample is $20 \pm 8\%$, $7 \pm 5\%$, and $9 \pm 5\%$ respectively. These are much smaller than that of the detection rate of Si III, although we note that in some sightlines the Si II λ 1260 Å was corrupted by the geocoronal O I emission feature and hence suffer from small number statistics. Our sensitivity is higher for Si III as compared to similar columns of Si II and Si IV. Therefore, a fair comparison is to compare the detection rate at the same column density. For example, we detected 6/31 ($16 \pm 7\%$) Si III absorbers with equivalent widths above the 0.077 \AA corresponding to a column density of $\text{Log } N(\text{Si III}) = 12.55$. At this same column density sensitivity, the detection rate of Si II is less than half that of Si III. However, the same argument cannot be applied to Si IV as our sensitivity

to Si IV is about an-order-of-magnitude lower, although none of the Si III absorbers have associated Si IV absorption.

Most of the Si III absorbers are tracing warm intermediate ionization circumgalactic gas. We find the observed line ratios of Si II, Si III, Si IV, and Lyman α from the COS-GASS sample to be consistent with photoionization of the CGM by the cosmic ultraviolet background. We expect the CGM in the outer halo as traced by Si III to have an ionization parameter, U , of $-2.8 < \log U < -1.7$, although the exact upper bound is hard to set given the saturation of Lyman α and non-detection of Si IV. Similar ionization parameters were also estimated by Shull et al. (2009) for Si III associated with the high- and intermediate-velocity clouds (HVC, IVC) in the Milky Way halo⁴. This value of ionization parameter is lower than required to produce a substantial amounts of O VI and C IV absorbers for the observed Lyman α column densities of $10^{14-15} \text{ atoms cm}^{-2}$ that are seen in our sample. And therefore, it is likely that most of these highly ionized absorbers are different from those detected in various other CGM and QSO-absorption studies (Tumlinson et al. 2011; Chen et al. 2001a; Wakker & Savage 2009; Borthakur et al. 2013; Bordoloi et al. 2014, and references therein). However, as discussed in detail by Werk et al. (2014); Fox et al. (2013); Meiring et al. (2013); Lehner et al. (2013); Tripp et al. (2011, and references therein), O VI may represent a different phase of gas that differs from the ones traced by lower ionization transitions. Since the COS-GASS data do not cover the O VI line, we refrain from further discussion of O VI. Instead, we focus on Lyman α and Si III in the remainder of the paper.

3.2. An Overview of the CGM Properties

We begin by summarizing the basic structural and kinematic properties of the CGM. Later, we will consider

³ It is worth noting that the study by Richter et al. (2016) is a statistical study of the Si III towards 303 QSO sightlines that may be associated with galaxies (instead of a targeted study of the CGM)

⁴ The conditions may not exactly be similar between the HVC/IVC and the COS-GASS absorbers since the HVC/IVC are within 50 kpc of the Milky Way disk (Lehner et al. 2012) and not the outer CGM (see Richter 2012; Herenz et al. 2013, for more on vantage point correction)

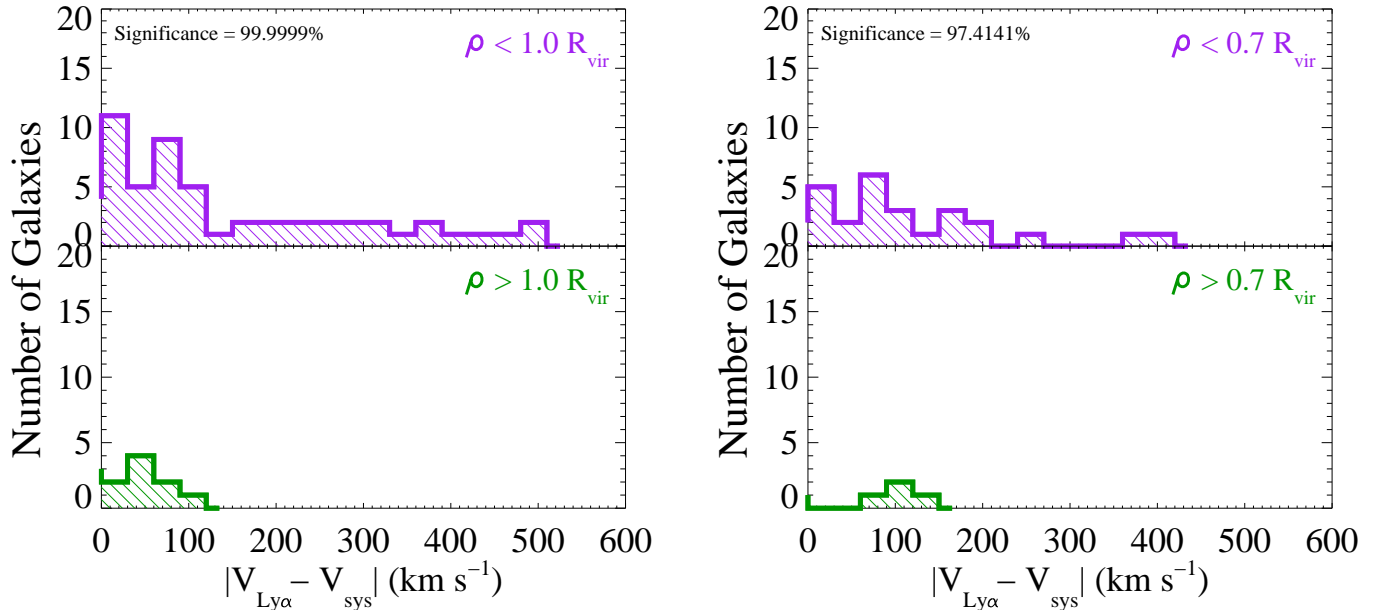


FIG. 9.— Left: Histogram showing the distribution of $|V_{\text{Ly}\alpha} - V_{\text{sys}}|$ for the sightlines probing the CGM of blue galaxies within R_{vir} and outside of R_{vir} . The ANOVA F-statistic test finds the two samples, the inner vs. the outer CGM, to have different Lyman α centroid velocities at a 99.99% confidence. Right: Histogram showing the distribution of $|V_{\text{Ly}\alpha} - V_{\text{sys}}|$ for the sightlines probing the CGM of red galaxies within $0.7 R_{\text{vir}}$ and outside of $0.7 R_{\text{vir}}$. The ANOVA F-statistic test finds the two samples, the inner vs. the outer CGM, to have different Lyman α centroid velocities at a 97.4% confidence.

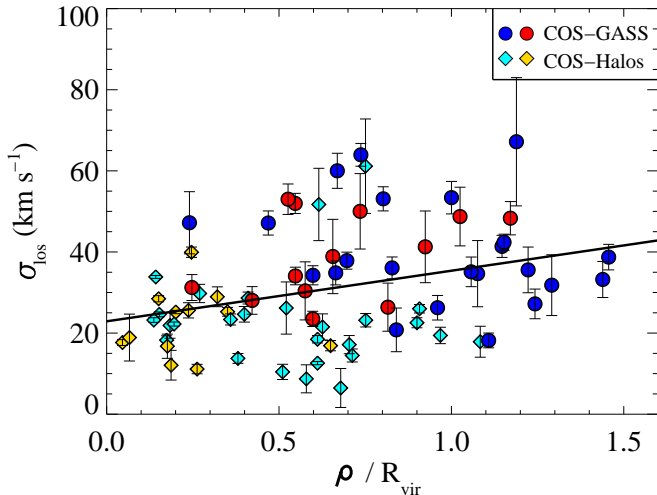


FIG. 10.— The line-of-sight velocity dispersion of the strongest component of the Lyman α absorption line plotted as a function of normalized impact parameter. The Kendall's τ test indicates a correlation that is significant at the 99.6% confidence level.

the dependence of these properties on the star forming characteristics of the central galaxy.

3.2.1. Structure

The dark matter halo mass of the galaxy should influence the size and kinematic properties of the CGM (Ford et al. 2016; Hummels et al. 2012, and references therein). For example, it is expected that a galaxy with a larger halo mass could contain a more massive CGM and gravitationally bind it to larger radii (Chen et al. 2001b). In order to explore the radial profile of the CGM

while accounting for the large range in halo mass, we use the variable ρ/R_{vir} , which we refer to as the normalized impact parameter (e.g. Stocke et al. 2013). This parameter scales the impact parameter (ρ) in terms of the size of the dark matter halo (R_{vir}). By doing so, we standardize the position of the sightlines for galaxies of different halo masses and consequently CGM sizes. Similar analyses have been performed on different data sets by Stocke et al. (2013) and Liang & Chen (2014), and on COS-Halos and COS-GASS by Tumlinson et al. (2013) and Borthakur et al. (2015) respectively.

We show the radial distribution of the equivalent width of Lyman α normalized with respect to the virial radius of the galaxies in Figure 2. The distribution can be fit as an exponential with a scale-length of $1.1 R_{\text{vir}}$, i.e. $W_{\text{Ly}\alpha} = A e^{-\rho/1.1R_{\text{vir}}} \text{ \AA}$, where the normalization factor, A , is equal to 0.9 \AA . The fit was derived using the Buckley-James⁵ method (Buckley & James 1979) and Expectation-maximization algorithm as implemented in the survival analysis software package, ASURV (Feigelson & Nelson 1985). The equivalent width data presented here are the same as that of Figure 2 of Borthakur et al. (2015), however, the abscissa is different as we have adopted the Kravtsov et al. (2014); Liang & Chen (2014) formalism with modifications based on the findings of Mandelbaum et al. (2016) for halo masses and virial radii. In addition, the fit presented here takes into account the censored data and hence has slightly different parameters.

Similarly, the radial distribution of the equivalent width of Si III (see right panel of Figure 2) can be fit as an exponential with a scale-length of $0.4 R_{\text{vir}}$ i.e. $W_{\text{SiIII}} = 0.4 e^{-\rho/0.4R_{\text{vir}}} \text{ \AA}$. Almost all of our Si III absorbers were detected inwards of $0.8R_{\text{vir}}$. The smaller

⁵ The Buckley-James method is a semi-parametric regression method

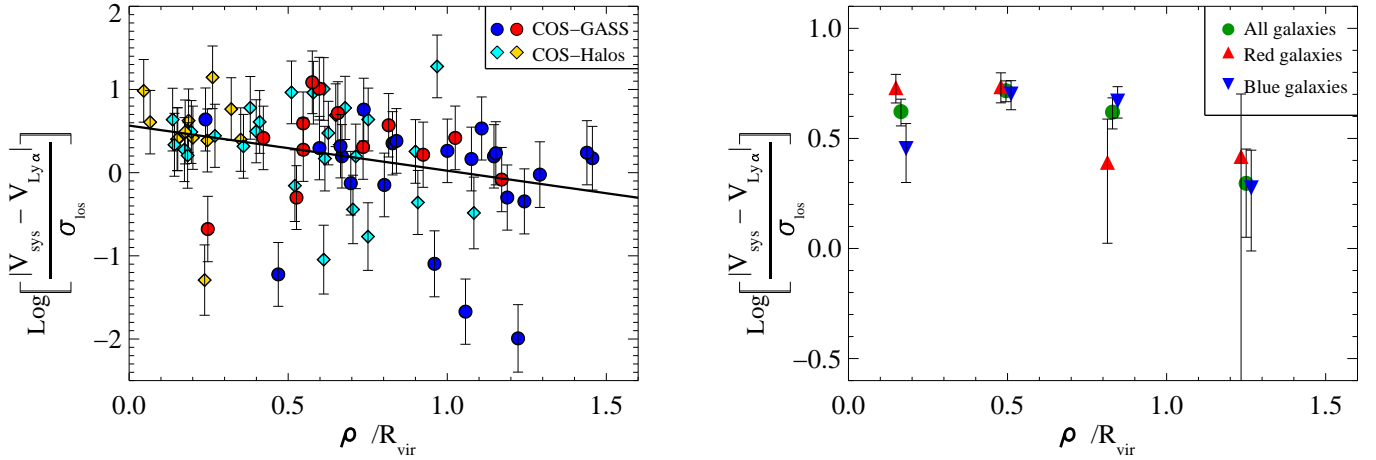


FIG. 11.— The log of the ratio of Δv (the velocity difference between the Lyman α absorption line and galaxy systemic velocity) and σ_{los} (the line-of-sight velocity dispersion) as a function of normalized impact parameter. The Kendall's τ test indicates that the correlation is significant at the 99.9% confidence level. The solid line is the best fit. The bottom panel shows the same relation but using the mean values in bins of normalized impact parameter. The drop in the ratio in the outer CGM is evident.

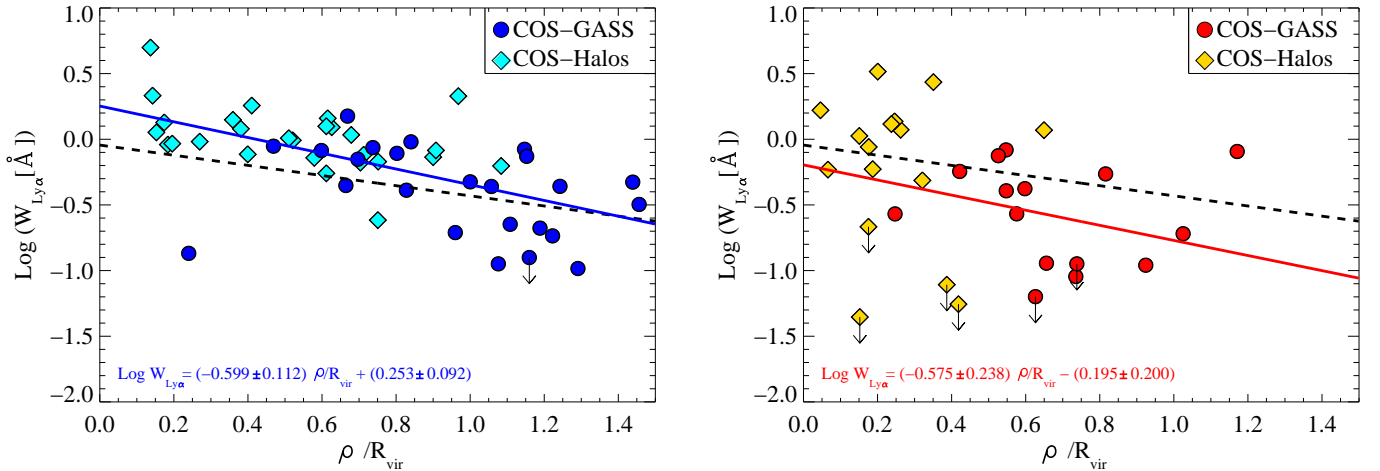


FIG. 12.— Variation of Lyman α equivalent width as a function of normalized impact parameter i.e. ρ/R_{vir} . The galaxies are divided into two classes, blue galaxies (left panels) and red galaxies (right panels), based on their sSFR being above or below $10^{-11} M_{\odot} \text{ yr}^{-1}$. The solid blue and red lines show the best-fit to the plotted data using the Buckley-James method. The fits were performed using the survival analysis software ASURV that takes into account the censored data. The dashed black line denotes the fit to the entire data set as shown in left panel of fig-2. The parameters describing the best-fit lines are printed at the bottom left corner.

characteristic size scale for the Si III absorbers compared to Lyman α and the lack of Si III detections beyond about $0.8 R_{vir}$ are consistent with the conclusions drawn by Liang & Chen (2014).

Given the systematic radial decline in the strengths of both the Lyman α and Si III absorbers, we define a new parameter: the impact parameter corrected equivalent width (hereafter, the excess equivalent width, $[\text{Log } W - \text{Log } \bar{W}]_{ion}$). This refers to the offset in $\text{Log } W_{ion}$ in any individual sightline with respect to the best fit exponential for the entire sample. This parameter is then independent of impact parameter biases and allows us to compare all the absorbers in a uniform way.

3.2.2. Kinematics

We turn now to the kinematic properties of the CGM. To begin, a useful way of visualizing these properties is via the one-dimensional cross-correlation function. The cross-correlation function between galaxies and velocity centroids of Lyman α absorbers is presented in the Figure 3. The cross-correlation function shows a strong signal for the presence of Lyman α absorbers within 120 km s^{-1} of the galaxy systemic velocity. The systemic velocity is defined as the velocity corresponding to the optical spectroscopic redshift from SDSS that traces the stars that form the bulk of the baryonic material in the central region of the galaxies.

The uncertainties were derived using a Jackknife error estimator and are indicated as the brown line. They are dominated by small number statistics although the random pairs were generated by using 10,000 Monte Carlo

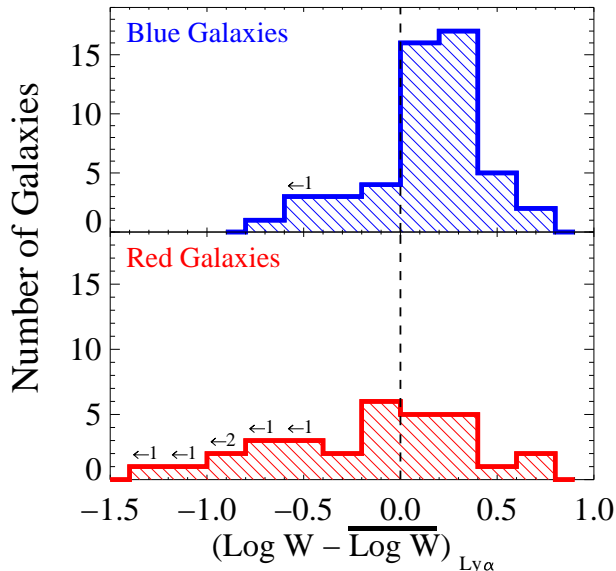


FIG. 13.— Distribution of $[\text{Log } W - \overline{\text{Log } W}]_{\text{Ly}\alpha}$ i.e. the offset in the Lyman α equivalent width from the best-fit line described in Figure 3 for the combined samples of blue and red galaxies. The black arrows refer to the limiting cases included in each bin. The Logrank test taking into account the censored data finds the two samples, blue galaxies and red galaxies, to differ in their Lyman α equivalent width at a confidence level of 99.9%.

samples. The cross-correlation function also takes into account the same data analysis criteria as the observations. For example, we have taken into account the observational aspect of identifying features by designating absorbers within $\pm 600 \text{ km s}^{-1}$ of the galaxy systemic as associated absorbers. For estimating the cross-correlation function, we randomly distributed the Lyman α absorbers within $\pm 600 \text{ km s}^{-1}$ of the galaxy systemic velocity. Therefore, it is not advisable to compare this analysis with blind galaxy-absorber cross-correlation functions such as those published by Lanzetta et al. (1998); Chen et al. (2005); Ryan-Weber (2006); Wilman et al. (2007); Chen & Mulchaey (2009); Tejos et al. (2012) and others. We also considered each component of the Lyman α absorption features as an individual absorber. This should be given due consideration when comparing our results to those from other studies that use spectrographs with significantly different velocity resolution from COS.

Similar conclusions can be drawn for the Si III transition. The distribution of Si III is also closely related to that of Lyman α absorption, although not all Lyman α absorbers have associated Si III absorption. To illustrate the velocity distribution of Si III with respect to Lyman α , we calculated the cross-correlation function between the velocity offset between Lyman α and Si III. In doing so, we preserved the relationship between distribution of Lyman α centroids w.r.t the galaxy systemic - which implies that Lyman α is not randomly distributed w.r.t $v = 0$. The cross-correlation function is presented in Figure 4. The red line indicates the cross-correlation function with the uncertainties shown in brown. The uncertainties were calculated using the same procedure as described previously. The correlation is strongest within $\pm 40 \text{ km s}^{-1}$ of the Lyman α absorbers and drops gradually. The signal-to-noise is greater than 3.5σ up to 160

km s^{-1} .

We now consider how the CGM kinematics depend upon the halo mass. Figure 5 shows the velocity offset of the absorbers relative to the systemic velocity of the galaxy ($|v_{\text{Ly}\alpha} - v_{\text{sys}}|$, hereafter Δv) plotted as a function of dark matter halo mass. We find that the velocity distribution of the centroids of majority of the Lyman α absorbers (as well as other detected metal absorbers) to typically lie within 200 km s^{-1} of the systemic velocity of the galaxy. The escape velocities at impact parameters of 100 kpc, 200 kpc, 300 kpc, and R_{vir} are plotted as dashed and solid curves of different colors. The centroids of the strongest component are shown as the filled symbols and the other components are shown as open symbols. The colored vertical lines connecting the strongest component to the other components mark the full-width of the Lyman α profiles. Nearly all the strongest Lyman α components have velocity centroids within the escape velocity of their host galaxies. Therefore, we expect this material to be bound to the galaxies.

Another way to characterize the kinematics of the CGM is to use the widths of the absorption features rather than their velocity displacement. In Figure 6 we plot the distribution of line-of-sight velocity dispersion of the strongest component of the Lyman α feature ($\sigma_{\text{los}} = b/\sqrt{2}$, where b is the Doppler parameter in our fits). Several features are noteworthy in this pair of figures. First, the lines are generally very narrow (mean $\sigma_{\text{los}} \sim 30 \text{ km s}^{-1}$). Second, there is no trend for these widths to increase as the halo mass (virial velocity) increases (as was also the case for Δv).

A compact representation of the information in the figures above is given in Figure 7. We define the kinematic parameter $W = (\sigma_{\text{bins}}^2 + \sigma_{\text{avg}}^2)^{1/2}$. Here, σ_{bins} is the velocity dispersion of the distribution of the velocity differences between the Lyman α absorber and the galaxy systemic velocities within a given bin in $\log M_{\text{halo}}$. The term σ_{avg} is the average value of σ_{los} of the individual Lyman α absorbers in this same bin in halo mass. Again, we see no dependence of CGM kinematics on halo mass. In particular, the low (sub-virial) velocity spread of CGM absorbers in the halos of massive red galaxies has been noted before (Zhu et al. 2014; Huang et al. 2016). We will discuss the possible implications of these results in section 4.

We can also examine the radial dependences of the CGM kinematics. In Figure 8 we plot the Lyman α velocity distribution as a function of normalized impact parameter. This figure suggests that the velocity offset of the absorbers from systemic velocity (Δv) drops in the outer CGM. The differing kinematic properties of the inner *vs.* the outer CGM are shown in histogram form in Figure 9. An F-test shows that the distributions differ at $>99.99\%$ (97.4%) confidence level for the blue (red) galaxies. In Figure 10 we show a similar plot of the radial dependence of the line-of-sight velocity dispersions (σ_{los}) of the Lyman α absorbers. This shows that there is a statistically significant (99.6% confidence level) trend for σ_{los} to increase with increasing impact parameter.

We next define the dimensionless quantity $\Delta v/\sigma_{\text{los}}$, and plot it in Figure 8 as a function of normalized impact parameter. The most interesting result is that $\Delta v/\sigma_{\text{los}}$ has a mean value of about four interior to the virial ra-

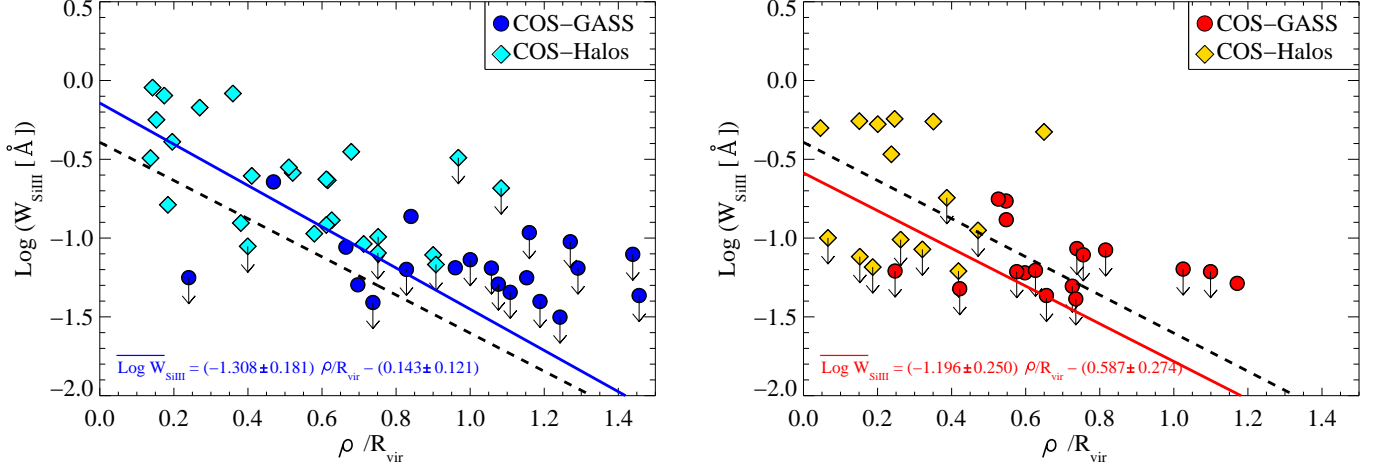


FIG. 14.— Variation of Si III equivalent width with normalized impact parameter i.e. ρ/R_{vir} . The galaxies are divided into two classes, red and blue, depending on whether the sSFR less or greater than $10^{-11} M_{\odot} \text{ yr}^{-1}$. The solid blue and red lines show the best-fit to the plotted data using the Buckley-James method. The fits were performed using the survival analysis software ASURV that takes into account the censored data. The dashed black line denotes the fit to the entire data set as shown in the right panel of fig-2. The parameters describing the best-fit lines are printed at the bottom left corner.

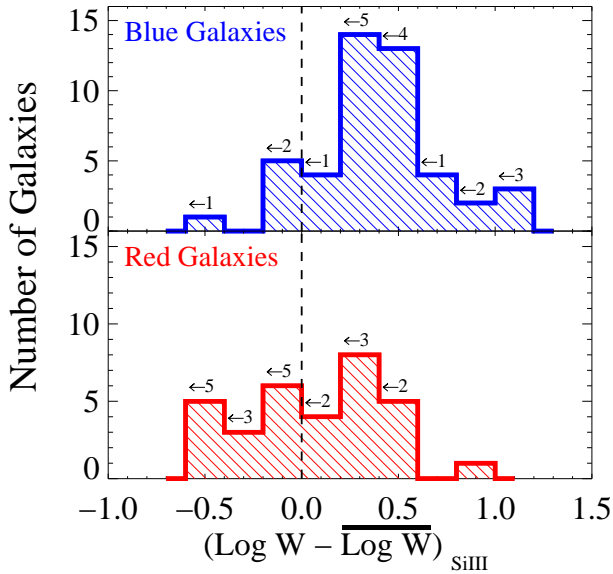


FIG. 15.— Distribution of $[\text{Log } W - \overline{\text{Log } W}]_{\text{SiIII}1206}$ i.e. the offset in the Si III equivalent width from the best-fit line described in Figure 3 for the blue and the red galaxies. The black arrows refers to the limiting cases included in each bin. The Logrank test taking into account the censored data finds the two samples, blue galaxies and red galaxies, to differ in their Si III equivalent width at slightly more than 99.8% confidence.

dius. This figure also shows that the ratio declines in the outer CGM (a result significant at the 99.9% confidence level). This is due to the combined effects of the drop in the Δv in the outer CGM and the radial rise in σ_{los} that were described above.

3.3. The CGM in Blue vs. Red Galaxies

We now compare the radial distributions of the absorbers in the CGM surrounding the blue *vs.* the red galaxies. The radial Lyman α profiles as a function of normalized impact parameter (ρ/R_{vir}) are shown in Figure 12. One clear difference is the dispersion in the data between the two sub-samples. The blue galaxies show a

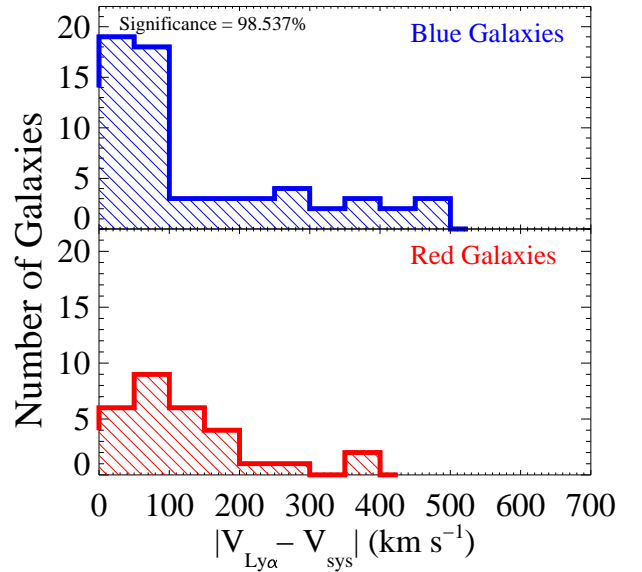


FIG. 16.— Histogram showing the distribution of $|V_{\text{Ly}\alpha} - V_{\text{sys}}|$ for the blue and the red galaxies. The ANOVA F-statistic test finds the two samples, blue galaxies and red galaxies, to have different Lyman α centroid velocity distributions at a 98.5% confidence level.

fairly uniform radial distribution with a $>95\%$ detection rate of Lyman α absorbers out to $\sim R_{\text{vir}}$. On the other hand, the red galaxies show a much larger dispersion in the radial distribution (as indicated by weak absorption features as well as non-detections with very good upper limits). It is worth noting that red galaxies do occasionally exhibit strong Lyman α absorbers associated with their CGM, but their detection rate is not as large as in blue galaxies. This is particularly true for the inner CGM, and suggests that the warm CGM is more patchy in the red galaxies (has a smaller areal covering factor).

The dashed black line is the fit to entire sample, whereas the blue and red solid lines are fits to blue and red galaxies respectively. The implied exponential scale-lengths for the blue and red galaxies are similar to one

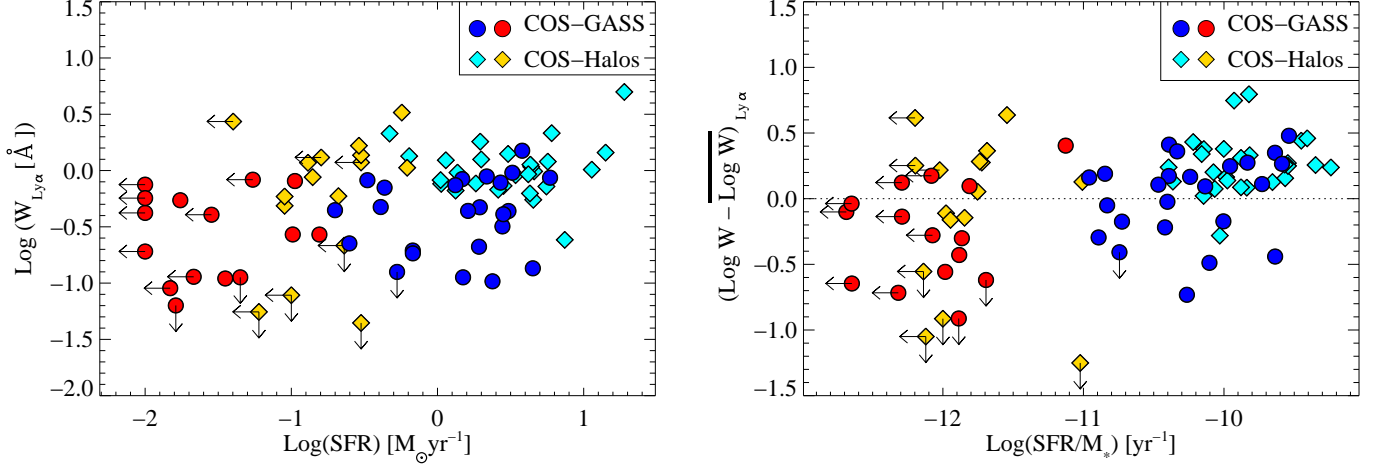


FIG. 17.— LEFT: Lyman α equivalent width as a function of star formation rate (SFR) of the host galaxy. RIGHT: Impact parameter corrected equivalent width $(\text{Log } W - \overline{\text{Log } W})_{\text{Ly}\alpha}$ as a function of specific SFR of the galaxies. Excess equivalent width is defined as the ratio of the observed Lyman α equivalent width and that predicted by the best fit line for the entire sample as shown in Figure 2. The correlation between the excess in equivalent width of Lyman α and sSFR is measured at the 99.99% confidence level using survival analysis code ASURV.

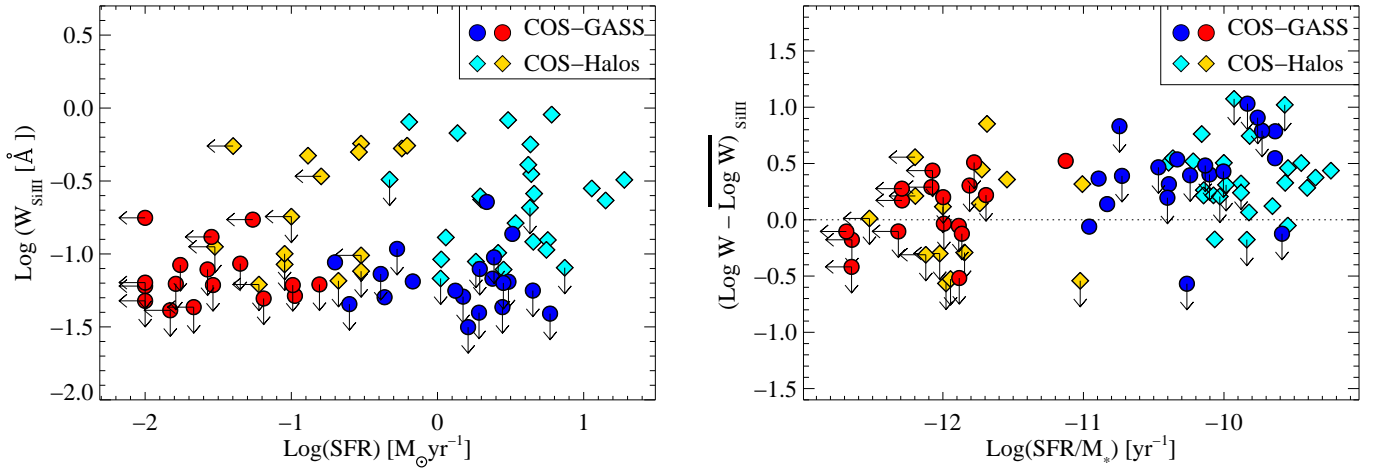


FIG. 18.— LEFT: Si III equivalent width as a function of star formation rate (SFR) of the host galaxy. RIGHT: The excess in Si III equivalent width $(\text{Log } W - \overline{\text{Log } W})_{\text{SiIII}1206}$ as a function of specific SFR of the galaxies. The excess in Si III equivalent width represents the difference between the observed Si III equivalent width and that predicted by the best fit line as shown in Figure 2. The correlation between the excess in equivalent width of Si III and sSFR is measured at the 99.7% confidence level using survival analysis code ASURV.

another ($0.65 R_{\text{vir}}$ and $0.75 R_{\text{vir}}$ respectively). The difference in the normalization of the profiles of 0.45 dex (blue vs. red) reflects the patchy nature of the absorbers in the CGM of the red galaxies.

Histogram representations of the excess Lyman α equivalent widths for the blue and red galaxies are presented in Figure 13. The dispersion in the red galaxy sub-sample is much higher than in the blue galaxy sub-sample. Again, this signifies the difference in the covering fraction of neutral gas between the two populations. The distribution in the excess Lyman α equivalent widths between the blue and red galaxies is significant such that these two sub-samples can be considered as different populations with 99.9% confidence based on Logrank test statistics using the software package ASURV.

We find similar results for Si III (Figure 14). The exponential scale lengths are similar for the blue and red

galaxies ($0.33 R_{\text{vir}}$ and $0.36 R_{\text{vir}}$ respectively). The normalization of the fit to the equivalent width radial distribution is 0.44 dex higher for the blue galaxies, which again reflects the patchy nature of the absorbers in the CGM of the red galaxies. The histogram showing the distributions of the excess Si III equivalent widths is shown in Figure 15. The difference in the distribution of the excess Si III equivalent width between the red and the blue galaxies is significant at the 99.8% confidence level.

By and large, the kinematic properties of the CGM are quite similar between the blue and red galaxies. However, one notable difference is highlighted in Figure 16, which shows histograms of Δv for the individual Lyman α absorbers. While in both samples, the majority of the values for Δv are less than 100 km s^{-1} , the blue galaxy histogram has a pronounced tail extending out to $\Delta v \sim 500 \text{ km s}^{-1}$. An Analysis of Variance (ANOVA) F-test reveals that the blue and red samples differ at the

98.5% confidence level.

3.4. Correlation Between CGM Properties and SFR

In the discussion above we have simply classified galaxies as star-forming (blue) or quiescent (red). In this section we focus on quantitative measures of the SFR and the sSFR. In our recent study, we found a strong correlation between the neutral hydrogen content in the interstellar medium of galaxies (traced by the 21 cm hyperfine transition) and the Lyman α equivalent width in the outer CGM probed by the COS-GASS sample (Borthakur et al. 2015). We also found correlations between Lyman α strengths and both SFR and sSFR, but these were significantly weaker than those with the H I 21 cm mass or mass fraction. Here, we reinvestigate the correlations with SFR and sSFR using the much larger combined sample that better covers the full radial range of the CGM.

As seen in Figure 17, we find a positive correlation between the equivalent width of the Lyman α absorbers and the SFR at the 99.8% confidence level. We find an even stronger correlation with the excess equivalent width $[\text{Log } W - \overline{\text{Log } W}]_{\text{Ly}\alpha}$ and the galaxy sSFR (at the 99.99% confidence level⁶). We also find similar correlations between SFR and the equivalent width of the Si III and between the excess Si III equivalent width $[\text{Log } W - \overline{\text{Log } W}]_{\text{SiIII}206}$ and sSFR (see Figure 18).

4. DISCUSSION

We want to highlight a number of the results above and try to connect them together into a simple picture of the warm ionized phase of the CGM in both the blue (star-forming) and red (quiescent) galaxies.

We have found that the distribution of Si III absorbers is more compact than that of the Lyman α absorbers for both the red and blue galaxies (with exponential length scales of ~ 0.35 vs. $0.7 R_{\text{vir}}$ for the respective ions in both the blue and red galaxies). As a consequence, the detection fraction of Si III for the full sample drops from 67% inside $0.7 R_{\text{vir}}$ to only 17% outside. This was also seen by Liang & Chen (2014), who interpreted it in terms of a boundary that represents the region that has been significantly enriched by metals expelled from the central galaxy (e.g. affected by stellar feedback at some point in the evolution of the galaxy and its CGM). We also see a change in the distribution of the velocity offsets between the Lyman α lines and galaxy systemic velocities in the outer CGM. While this could be related to feedback processes, it could also be due to line-of-sight projection effects, if the flow pattern in the CGM has a strong radial component (inward and/or outward).

Perhaps the most surprising result is that in neither the red nor blue populations do we see any trend for either the velocity offset of the Lyman α absorbers with respect to the galaxy systemic velocity (Δv) or the line-of-sight

velocity dispersions (σ_{los}) of the absorption lines to increase with increasing halo mass across a range of about 5 in implied virial velocity. The implied sub-virial velocities in the CGM around massive red galaxies have been noted before (Zhu et al. 2014; Huang et al. 2016), and are particularly mysterious. One possibility is that we are seeing the condensation of thermal instabilities out of a hot volume-filling phase (Voit et al. 2015). The hot gas is supported hydrostatically, and the denser cooler clouds that condense out have not (yet) been accelerated by gravity to the virial velocity of the halo. This would suggest that these clouds in massive red galaxies are transient (lifetimes less than a halo crossing time).

Another possibility is that the flow of the absorbing material in the warm CGM of these galaxies is significantly affected by drag forces associated with a more massive hot volume-filling phase. In any case, it appears that the CGM dynamics are not purely determined by gravitational forces alone. Since we expect that the absorption-line systems we see are imbedded in a multi-phase halo, their dynamics is likely to be influenced by processes such as drag forces, thermal instabilities, turbulent mixing, merger dynamics, and feedback-driven outflows (Maller & Bullock 2004; Santillan et al. 2007; Kwak & Shelton 2010; Kwak et al. 2011; Joung et al. 2012a,b; Stinson et al. 2012; Ford et al. 2014; Fielding et al. 2016; Suresh et al. 2015).

The role of drag forces in reducing the velocities of the CGM clouds in massive halos is particularly interesting to consider. Following Bordoloi et al. (2016), it is straightforward to show that the terminal velocity for a CGM cloud that is significantly affected by drag is given by:

$$v_{\text{term}} \sim v_{\text{vir}}(M_{\text{cs}}/M_{\text{vf}})^{1/2} \quad (1)$$

Here v_{vir} is the virial velocity of the halo, and M_{vf} and M_{cs} are the total masses of the volume-filling gas and the system of clouds in the CGM. For drag forces to be important, the volume-filling phase needs to significantly exceed the total cloud mass. The amount of mass in a volume-filling phase is uncertain in typical Milky Way-like galaxies (e.g. Miller & Bregman 2013), but appears to be significant in the halos of more massive galaxies (Planck Collaboration et al. 2013; Greco et al. 2015).

We also find that the ratio $\Delta v/\sigma_{\text{los}}$ is typically large (mean value of ~ 4 , see Figure 11) interior to the virial radius. This is true in both the blue and red galaxies. This result is inconsistent with at least one simple and otherwise plausible model in which a single line-of-sight through the CGM intersects many clouds with distinct locations and a wide range of line-of-sight velocities (e.g. a sea of clouds orbiting in the halo potential). Instead it implies that a typical line-of-sight through the CGM is intersecting a coherent structure (a cloud, sheet, or filament). Current constraints on the size of these structures (which are based on models in which the gas is photoionized by the meta-galactic background) are rather weak, but characteristic path-lengths are of-order 1 to 10 kpc (Stocke et al. 2013; Werk et al. 2014).

Despite many of the similarities between the CGM in red and blue galaxies noted above, we do find significant differences. First, in terms of the radial distributions of the Lyman α and Si III equivalent widths, the red

⁶ The test was performed on our censored data using the astronomy survival analysis code ASURV (Feigelson & Nelson 1985). ASURV is capable of handling single and doubly censored data. The accuracy of these probabilities can be affected by larger numbers of censored values and other conditions. Since less than a quarter of our sample has censored values, we do not expect substantial inaccuracies. However, caution is appropriate as is for results from Kendall's test on any sample (Wang & Wells 2000).

galaxies have lower normalizations for the exponential fits, reflecting a patchy distribution of absorbers. There is also a significant fraction of the blue galaxies showing large velocity differences between the radial velocity of the absorber and central galaxy (Δv up to 500 km s^{-1}). Taken together with the COS-Halos results on the presence (absence) of highly ionized gas (seen as O VI absorbers Tumlinson et al. 2011) in blue (red) galaxies, there are therefore real differences between the CGM surrounding star-forming and quiescent galaxies. Unfortunately, as discussed in Section 3.1, the data from the COS-GASS do not cover O VI, and thus we are not able to do the same analysis as done by Tumlinson et al. (2011) for the combined sample.

The interpretation of these differences is not straightforward. The direction of the causal connection between the properties of the CGM and the galaxy could be in either direction (or both). The CGM properties could be influenced by feedback from the galaxy, and the amount and nature of this could be significantly different between the blue and red galaxies (e.g. feedback from massive stars and supernovae *vs.* feedback associated with AGN-driven radio sources (“radio mode”). Alternatively, or in addition, the star-forming properties of the galaxies may be driven by the different observed properties of the CGM.

One of the main motivations of this paper were to understand whether and how the properties of the CGM in star-forming and quiescent galaxies relate to the cessation of star-formation in the latter. The results we have presented seem to imply rather subtle differences between the two types of galaxies. Here, we will argue that the apparently subtle differences could have significant implications.

Let us consider a simple model in which the star-formation rate in a given galaxy is proportional to the total mass of the system of CGM clouds traced by the absorption-lines (M_{cs}) divided by the timescale for these clouds to be transported from the CGM to the galaxy ($t_{in} \propto R_{vir}/v_{in}$). The results in Figure 2 imply that $M_{cs} \propto f_c R_{vir}^2$, where f_c is the fraction of the cross-sectional area of the CGM (πR_{vir}^2) covered by these clouds. Empirically, we see no dependence of the cloud kinematics on the mass of the dark matter halo. Hence, we will assume that v_{in} is likewise independent of M_{halo} . Taken together this implies that the specific star-formation rate scales as $sSFR \propto f_c R_{vir}^2 / R_{vir} M_* \propto f_c R_{vir} / M_*$. Using our adopted scaling between M_* and R_{vir} , the predicted value of sSFR drops by a factor of ten with increasing stellar mass over the range in $M_* = 10^{10.0}$ to $10^{11.5} M_\odot$, even if f_c does not change. Given that f_c is a factor of 3 smaller in the red galaxies (Figures 12 and 14), this simple model then predicts a difference in the sSFR between the lowest-mass blue galaxies and highest-mass red galaxies in our sample of a factor of 30.

Of course this model is purely phenomenological and does not explain the scaling of M_c with R_{vir} or the invariance in v_{in} . These relations are simply based on the observations. One possible interpretation would be that the mass of the population of clouds relative to that of the hot diffuse volume-filling CGM phase drops as a function of M_{halo} . This reduces the normalized mass of the reservoir of clouds (M_{cs}/M_*) and increases the transport

time of the clouds to the galaxy with increasing mass due to increasing drag forces. Such an idea is at least qualitatively consistent with the simple paradigm of a transition from predominantly cold accretion to a quasi-hydrostatic hot CGM as halo and galaxy mass increases.

5. SUMMARY

We have presented the analysis of a comprehensive data set combining the COS-GASS and COS-Halos samples to probe the CGM of low- z galaxies spanning a stellar mass range of almost two orders-of-magnitude centered on the characteristic mass ($\sim 10^{10.5} M_\odot$) at which the galaxy population transitions from mostly blue, star-forming galaxies to red, quiescent ones. These two surveys cover similar ranges in stellar masses and dark halo virial radii (R_{vir}). In addition, the combined sample uniformly samples a large range of radial distances from 0.02 to $1.3 R_{vir}$. The COS-GASS survey primarily samples the outer CGM and COS-Halos survey primarily samples the inner CGM. We characterized the CGM properties, including its radial profile, its kinematics, and its correlation with the global properties of the galaxies. In particular we have divided the sample into blue galaxies (with $sSFR > 10^{-11} M_\odot \text{ yr}^{-1}$) and red galaxies (with lower sSFR).

In this analysis, we discussed the Lyman α $\lambda 1215\text{\AA}$ and Si III $\lambda 1206\text{\AA}$ transitions tracing intermediate ionization gas. Si III was chosen as it is the strongest metal transition detected in the combined data set. The typical detection limit for the COS-GASS sample is $\sim 50 \text{ m\AA}$ corresponding to 3σ uncertainty in the data. In the combined sample, the detection rates of Lyman α and Si III were 91% and $\sim 50\%$ respectively.

Based on the analysis of the combined sample we conclude the following:

1. The radial distribution of the equivalent width of Lyman α as a function of normalized impact parameter (ρ/R_{vir}) can be expressed as an exponential. The scale-lengths are similar for the red and blue galaxies (0.75 and $0.72 R_{vir}$ respectively). The radial distribution of equivalent width of Si III can also be expressed as an exponential with a scale-length of 0.36 (0.33) R_{vir} for the red (blue) galaxies. The detection rate of Si III drops to almost zero beyond about $0.8 R_{vir}$.
2. The blue galaxies show a relatively uniform radial distribution of Lyman α absorbers, implying an areal covering fraction of nearly 100% in the CGM. In contrast, the Lyman α absorbers have a much less uniform radial distribution in the CGM of the red galaxies, suggesting a patchy distribution with smaller areal covering fractions. These differences are reflected in the overall normalization of the radial distribution of equivalent widths, which is higher for the blue galaxies (by 0.45 dex). Similar results were found for Si III, but are restricted to the region interior to $0.8 R_{vir}$ (where Si III is detected).
3. We found a significant positive correlation between the equivalent width of Lyman α and the star-formation rate (at the 99.8% confidence level). The

correlation is even more significant for normalized quantities: the impact-parameter-corrected equivalent width of Lyman α ($[\text{Log } W - \overline{\text{Log } W}]_{\text{Ly}\alpha}$) and the specific SFR (SFR/M_*) were found to correlate at the 99.99% confidence level. Similar results were found for Si III.

4. We found the velocity distribution of the centroids of the majority of the Lyman α and Si III to generally lie within $\sim 150 \text{ km s}^{-1}$ of the systemic velocity of the galaxy. These velocities are smaller than the escape velocity, thus suggesting the gas seen in absorption is gravitationally bound within the halo. The metal-line transitions are also found mostly within $\pm 100 \text{ km s}^{-1}$ of Lyman α absorbers, although not all strong ($> 0.3\text{\AA}$) Lyman α absorbers showed associated Si III.
5. We find that the velocity offset between the Lyman α centroid and the systemic velocity (Δv) is usually significantly larger than the line-of-sight velocity dispersion of the Lyman α line (σ_{los}). The mean ratio $\Delta v/\sigma_{los} \sim 4$.
6. We find no dependence of the kinematic properties of the CGM (Δv or σ_{los}) on the galaxy halo mass (virial velocity). This is surprising, as the sample spans ranges of about 10^2 in halo mass and ~ 5 in v_{vir} .
7. We found that the kinematic properties of the CGM are generally similar between the blue and red galaxies. However, while the majority of both the blue and red galaxies have $\Delta v < 100 \text{ km s}^{-1}$, the distribution of Δv for the blue galaxies shows a pronounced tail out to values as high as 500 km s^{-1} .
8. We found a significant change in the CGM kinematics at about a radius of 1.0 (0.7) R_{vir} for the blue (red) galaxies. In the outer CGM Δv for the Lyman α absorbers is always less than 150 km s^{-1} , while the distributions of Δv show tails out to values as high as 500 km s^{-1} in the inner CGM. In addition, σ_{los} is higher on average in the outer CGM for both the blue and red galaxies. These two results lead to a corresponding decrease in $\Delta v/\sigma_{los}$ in the outer CGM.

The combined COS-GASS and COS-Halos sample has allowed us to conduct a comprehensive study of the connection of the properties of the CGM with those of the stellar body of the galaxy. We think that three of the specific results from above are particularly noteworthy. First, the differences in the radial distributions of the Lyman α vs. the Si III absorbers, suggest that the inner CGM is being (or has at some time been) affected by feedback associated with massive stars and supernovae. This feedback has chemically-enriched the CGM. It is interesting that the kinematics of the inner and outer CGM also show differences, although it is not clear that these are related to feedback or to projection effects.

Secondly, the fact that the typical ratio of the velocity offset to the line-of-sight velocity dispersion for the Lyman α absorption-lines is so large is an important clue

as to the structure of the CGM. It implies that a line-of-sight through the CGM does not intersect a whole sea of many clouds orbiting in the halo, but is rather passing through a coherent structure (cloud, sheet, filament). Model-dependent estimates imply a path-length of order 1 to 10 kpc for these structures.

Thirdly, the independence of the kinematic properties of the warm CGM on the halo mass is quite remarkable. This implies that, even though the observed absorption-line systems are mostly gravitationally bound to the halo, simple gravitational forces alone do not adequately explain the CGM dynamics. For the massive red galaxies, the “sub-virial” velocities could be understood if the absorbers represent material cooling and condensing out of (or suffering drag as they move through) a hot volume-filling phase that is supported hydrostatically against gravity.

A major motivation of this study was to understand how and why galaxies in this stellar mass regime exhibit the color bimodality stemming from a suppression/cessation of star-formation in some of them. Since the CGM is the interface through which galaxies could exchange gas and energy that is required to form stars (or is expelled as a result of star-formation), the CGM properties could hold clues as to how this process of gas delivery may be disrupted leaving some galaxies deprived of fuel to form stars. We have explored a simple scenario in which the star-formation rate in a galaxy is proportional to the total mass of CGM clouds divided by an inflow time. We then show that the empirical results on the independence of CGM kinematic properties on halo mass and the smaller covering factor in the CGM in the red galaxies would imply a drop in the specific star formation rate by about a factor of 30 over the stellar mass range from 10^{10} to $10^{11.5} M_{\odot}$.

In any event, we believe the data we have presented here provide a valuable observational resource for ongoing and future numerical simulations that try to reproduce CGM properties such as Lyman α and metal-line column density profiles, covering fraction, and dynamics, such as line-widths and velocity spreads (for example Hummels et al. 2012; Stinson et al. 2012; Shen et al. 2013; Ford et al. 2013, 2014, 2016; Liang et al. 2016; Kauffmann et al. 2016; Fielding et al. 2016, and references therein). The ultimate goal is understanding the role of the CGM in the evolution of galaxies.

We thank the referee for his useful comments. We thank Hsiao-Wen Chen, Cameron Hummels, Colin Norman, Josh Peek, Molly Peebles, Jason X. Prochaska, John Stocke, and Jessica Werk for helpful discussions. This work is based on observations with the NASA/ESA Hubble Space Telescope, which is operated by the Association of Universities for Research in Astronomy, Inc., under NASA contract NAS5-26555. SB and TH were supported by grant HST GO 12603. BC gratefully acknowledges support from the Australian Research Council’s Future Fellowship (FT120100660) and Discovery Project (DP150101734) funding schemes.”

This project also made use of SDSS data. Funding for the SDSS and SDSS-II has been provided by the Alfred P. Sloan Foundation, the Participating Institutions,

the National Science Foundation, the U.S. Department of Energy, the National Aeronautics and Space Administration, the Japanese Monbukagakusho, the Max Planck Society, and the Higher Education Funding Council for England. The SDSS Web Site is <http://www.sdss.org/>. The SDSS is managed by the Astrophysical Research Consortium for the Participating Institutions. The Participating Institutions are the American Museum of Natural History, Astrophysical Institute Potsdam, University of Basel, University of Cambridge, Case Western Reserve University, University of Chicago, Drexel University, Fermilab, the Institute for Advanced Study, the

Japan Participation Group, Johns Hopkins University, the Joint Institute for Nuclear Astrophysics, the Kavli Institute for Particle Astrophysics and Cosmology, the Korean Scientist Group, the Chinese Academy of Sciences (LAMOST), Los Alamos National Laboratory, the Max-Planck-Institute for Astronomy (MPIA), the Max-Planck-Institute for Astrophysics (MPA), New Mexico State University, Ohio State University, University of Pittsburgh, University of Portsmouth, Princeton University, the United States Naval Observatory, and the University of Washington.

Facilities: Sloan () HST (COS)

REFERENCES

- Baldry, I. K., Glazebrook, K., Brinkmann, J., et al. 2004, *ApJ*, 600, 681
- Blanton, M. R., Hogg, D. W., Bahcall, N. A., et al. 2003, *ApJ*, 592, 819
- Bordoloi, R., Heckman, T. M., & Norman, C. A. 2016, *ArXiv e-prints*
- Bordoloi, R., Tumlinson, J., Werk, J. K., et al. 2014, *ApJ*, 796, 136
- Borthakur, S., Heckman, T., Strickland, D., Wild, V., & Schiminovich, D. 2013, *ApJ*, 768, 18
- Borthakur, S., Heckman, T. M., Leitherer, C., & Overzier, R. A. 2014, *Science*, 346, 216
- Borthakur, S., Heckman, T., Tumlinson, J., et al. 2015, *ApJ*, 813, 46
- Bouché, N., Murphy, M. T., Kacprzak, G. G., et al. 2013, *Science*, 341, 50
- Bowen, D. V., Pettini, M., & Blades, J. C. 2002, *ApJ*, 580, 169
- Brinchmann, J., Charlot, S., White, S. D. M., et al. 2004a, *MNRAS*, 351, 1151
- . 2004b, *MNRAS*, 351, 1151
- Brook, C. B., Stinson, G., Gibson, B. K., et al. 2014, *MNRAS*, 443, 3809
- Buckley, J. J., & James, I. R. 1979, *Biometrika*, 66, 429
- Catinella, B., Schiminovich, D., Kauffmann, G., et al. 2010, *MNRAS*, 403, 683
- . 2012, *A&A*, 544, A65
- Catinella, B., Schiminovich, D., Cortese, L., et al. 2013, *MNRAS*, 436, 34
- Chen, H.-W. 2012, *MNRAS*, 427, 1238
- Chen, H.-W., Lanzetta, K. M., & Webb, J. K. 2001a, *ApJ*, 556, 158
- Chen, H.-W., Lanzetta, K. M., Webb, J. K., & Barcons, X. 1998, *ApJ*, 498, 77
- . 2001b, *ApJ*, 559, 654
- Chen, H.-W., & Mulchaey, J. S. 2009, *ApJ*, 701, 1219
- Chen, H.-W., Prochaska, J. X., Weiner, B. J., Mulchaey, J. S., & Williger, G. M. 2005, *ApJ*, 629, L25
- Collins, J. A., Shull, J. M., & Giroux, M. L. 2009, *ApJ*, 705, 962
- Daddi, E., Dickinson, M., Morrison, G., et al. 2007, *ApJ*, 670, 156
- Dekel, A., Birnboim, Y., Engel, G., et al. 2009, *Nature*, 457, 451
- Feigelson, E. D., & Nelson, P. I. 1985, *ApJ*, 293, 192
- Fernández, X., Joung, M. R., & Putman, M. E. 2012, *ApJ*, 749, 181
- Fielding, D., Quataert, E., McCourt, M., & Thompson, T. A. 2016, *ArXiv e-prints*
- Ford, A. B., Davé, R., Oppenheimer, B. D., et al. 2014, *MNRAS*, 444, 1260
- Ford, A. B., Oppenheimer, B. D., Davé, R., et al. 2013, *MNRAS*, 432, 89
- Ford, A. B., Werk, J. K., Davé, R., et al. 2016, *MNRAS*, 459, 1745
- Fox, A. J., Lehner, N., Tumlinson, J., et al. 2013, *ApJ*, 778, 187
- Fraternali, F., Marasco, A., Armillotta, L., & Marinacci, F. 2015, *MNRAS*, 447, L70
- Fukugita, M., & Peebles, P. J. E. 2006, *ApJ*, 639, 590
- Greco, J. P., Hill, J. C., Spergel, D. N., & Battaglia, N. 2015, *ApJ*, 808, 151
- Grieb, J. N., Sánchez, A. G., Salazar-Albornoz, S., et al. 2016, *ArXiv e-prints*
- Heckman, T. M., Alexandroff, R. M., Borthakur, S., Overzier, R., & Leitherer, C. 2015, *ApJ*, 809, 147
- Heckman, T. M., & Borthakur, S. 2016, *ApJ*, 822, 9
- Heckman, T. M., Borthakur, S., Overzier, R., et al. 2011, *ApJ*, 730, 5
- Herenz, P., Richter, P., Charlton, J. C., & Masiero, J. R. 2013, *A&A*, 550, A87
- Huang, Y.-H., Chen, H.-W., Johnson, S. D., & Weiner, B. J. 2016, *MNRAS*, 455, 1713
- Hummels, C., Bryan, G., Smith, B., & Turk, M. 2012, *ArXiv e-prints*
- Joung, M. R., Bryan, G. L., & Putman, M. E. 2012a, *ApJ*, 745, 148
- Joung, M. R., Putman, M. E., Bryan, G. L., Fernández, X., & Peek, J. E. G. 2012b, *ApJ*, 759, 137
- Kauffmann, G., Borthakur, S., & Nelson, D. 2016, *MNRAS*
- Kauffmann, G., Heckman, T. M., White, S. D. M., et al. 2003, *MNRAS*, 341, 33
- Kaufmann, T., Bullock, J. S., Maller, A. H., Fang, T., & Wadsley, J. 2009, *MNRAS*, 396, 191
- Kaufmann, T., Mayer, L., Wadsley, J., Stadel, J., & Moore, B. 2006, *MNRAS*, 370, 1612
- Kereš, D., & Hernquist, L. 2009, *ApJ*, 700, L1
- Kereš, D., Katz, N., Fardal, M., Davé, R., & Weinberg, D. H. 2009, *MNRAS*, 395, 160
- Kereš, D., Katz, N., Weinberg, D. H., & Davé, R. 2005, *MNRAS*, 363, 2
- Kravtsov, A., Vikhlinin, A., & Meshcheryakov, A. 2014, *ArXiv e-prints*
- Kwak, K., Henley, D. B., & Shelton, R. L. 2011, *ApJ*, 739, 30
- Kwak, K., & Shelton, R. L. 2010, *ApJ*, 719, 523
- Lanzetta, K. M., Bowen, D. V., Tytler, D., & Webb, J. K. 1995, *ApJ*, 442, 538
- Lanzetta, K. M., Webb, J. K., & Barcons, X. 1998, in *Astronomical Society of the Pacific Conference Series*, Vol. 146, *The Young Universe: Galaxy Formation and Evolution at Intermediate and High Redshift*, ed. S. D’Odorico, A. Fontana, & E. Giallongo, 175
- Lehner, N., Howk, J. C., Thom, C., et al. 2012, *MNRAS*, 424, 2896
- Lehner, N., Howk, J. C., & Wakker, B. P. 2015, *ApJ*, 804, 79
- Lehner, N., Howk, J. C., Tripp, T. M., et al. 2013, *ApJ*, 770, 138
- Liang, C. J., & Chen, H.-W. 2014, *MNRAS*, 445, 2061
- Liang, C. J., Kravtsov, A. V., & Agertz, O. 2016, *MNRAS*, 458, 1164
- Maller, A. H., & Bullock, J. S. 2004, *MNRAS*, 355, 694
- Mandelbaum, R., Wang, W., Zu, Y., et al. 2016, *MNRAS*, 457, 3200
- Marasco, A., Debattista, V. P., Fraternali, F., et al. 2015, *MNRAS*, 451, 4223
- Meiring, J. D., Tripp, T. M., Werk, J. K., et al. 2013, *ApJ*, 767, 49
- Miller, M. J., & Bregman, J. N. 2013, *ApJ*, 770, 118
- Mitra, S., Davé, R., & Finlator, K. 2015, *MNRAS*, 452, 1184
- Moran, S. M., Heckman, T. M., Kauffmann, G., et al. 2012, *ApJ*, 745, 66
- Nelson, D., Genel, S., Pillepich, A., et al. 2016, *MNRAS*, 460, 2881
- Nelson, D., Genel, S., Vogelsberger, M., et al. 2015, *MNRAS*, 448, 59
- Nielsen, N. M., Churchill, C. W., Kacprzak, G. G., Murphy, M. T., & Evans, J. L. 2015, *ApJ*, 812, 83
- Noeske, K. G., Weiner, B. J., Faber, S. M., et al. 2007, *ApJ*, 660, L43
- Peebles, M. S., Werk, J. K., Tumlinson, J., et al. 2014, *ApJ*, 786, 54

- Planck Collaboration, Ade, P. A. R., Aghanim, N., et al. 2013, *A&A*, 557, A52
- Prochaska, J. X., Weiner, B., Chen, H.-W., Mulchaey, J., & Cooksey, K. 2011, *ApJ*, 740, 91
- Richter, P. 2012, *ApJ*, 750, 165
- Richter, P., Wakker, B. P., Fechner, C., et al. 2016, *A&A*, 590, A68
- Riess, A. G., Macri, L. M., Hoffmann, S. L., et al. 2016, *ApJ*, 826, 56
- Rodighiero, G., Daddi, E., Baronchelli, I., et al. 2011, *ApJ*, 739, L40
- Ryan-Weber, E. V. 2006, *MNRAS*, 367, 1251
- Saintonge, A., Kauffmann, G., Kramer, C., et al. 2011, *MNRAS*, 415, 32
- Salim, S., Rich, R. M., Charlot, S., et al. 2007, *ApJS*, 173, 267
- Santillan, A., Hernandez-Cervantes, L., Gonzalez-Ponce, A., & Kim, J. 2007, *Journal of Korean Astronomical Society*, 40, 165
- Shen, S., Madau, P., Conroy, C., Governato, F., & Mayer, L. 2014, *ApJ*, 792, 99
- Shen, S., Madau, P., Guedes, J., et al. 2013, *ApJ*, 765, 89
- Shull, J. M., Jones, J. R., Danforth, C. W., & Collins, J. A. 2009, *ApJ*, 699, 754
- Snyder, G. F., Torrey, P., Lotz, J. M., et al. 2015, *MNRAS*, 454, 1886
- Somerville, R. S., & Davé, R. 2015, *ARA&A*, 53, 51
- Sommer-Larsen, J. 2006, *ApJ*, 644, L1
- Speagle, J. S., Steinhardt, C. L., Capak, P. L., & Silverman, J. D. 2014, *ApJS*, 214, 15
- Stinson, G. S., Brook, C., Prochaska, J. X., et al. 2012, *MNRAS*, 425, 1270
- Stocke, J. T., Keeney, B. A., Danforth, C. W., et al. 2013, *ApJ*, 763, 148
- Suresh, J., Bird, S., Vogelsberger, M., et al. 2015, *MNRAS*, 448, 895
- Tejos, N., Morris, S. L., Crighton, N. H. M., et al. 2012, *MNRAS*, 425, 245
- Tripp, T. M., Lu, L., & Savage, B. D. 1998, *ApJ*, 508, 200
- Tripp, T. M., Meiring, J. D., Prochaska, J. X., et al. 2011, *Science*, 334, 952
- Tully, R. B., Mould, J. R., & Aaronson, M. 1982, *ApJ*, 257, 527
- Tumlinson, J., Thom, C., Werk, J. K., et al. 2011, *Science*, 334, 948
- . 2013, *ApJ*, 777, 59
- Veilleux, S., Cecil, G., & Bland-Hawthorn, J. 2005, *ARA&A*, 43, 769
- Voit, G. M., Donahue, M., Bryan, G. L., & McDonald, M. 2015, *Nature*, 519, 203
- Wakker, B. P., & Savage, B. D. 2009, *ApJS*, 182, 378
- Wang, W., & Wells, M. T. 2000, *Statistica Sinica*, 10, 1199
- Werk, J. K., Prochaska, J. X., Thom, C., et al. 2013, *ApJS*, 204, 17
- Werk, J. K., Prochaska, J. X., Tumlinson, J., et al. 2014, *ApJ*, 792, 8
- White, S. D. M., & Frenk, C. S. 1991, *ApJ*, 379, 52
- Wilman, R. J., Morris, S. L., Jannuzi, B. T., Davé, R., & Shone, A. M. 2007, *MNRAS*, 375, 735
- Yang, X., Mo, H. J., van den Bosch, F. C., & Jing, Y. P. 2005, *MNRAS*, 356, 1293
- Yang, X., Mo, H. J., van den Bosch, F. C., et al. 2007, *ApJ*, 671, 153
- Zhu, G., Ménard, B., Bizyaev, D., et al. 2014, *MNRAS*, 439, 3139

TABLE 1
DESCRIPTION OF GALAXY PROPERTIES FOR THE COS-GASS SURVEY^a.

Galaxy	GASS ID	RA	Dec	z_{gal}	M_{\star} (Log M_{\odot})	$M_{\text{halo}}^{\text{b}}$ (Log M_{\odot})	$R_{\text{vir}}^{\text{c}}$ (kpc)	sSFR (Log yr ⁻¹)	Color ^d	$v_{\text{esc,Rvir}}^{\text{e}}$ (km s ⁻¹)
J0159+1346	3936	29.941	13.781	0.0441	10.1	11.4	153	-9.5	Blue	114
J0808+0512	19852	122.068	5.216	0.0308	10.8	12.2	296	-12.0	Red	217
J0852+0309	8096	133.229	3.152	0.0345	10.3	11.5	166	-10.1	Blue	122
J0908+3234	22391	137.232	32.576	0.0490	10.5	11.9	232	-12.3	Red	174
J0914+0836	20042	138.684	8.601	0.0468	10.0	11.3	147	-9.6	Blue	110
J0930+2853	32907	142.538	28.898	0.0349	10.5	11.6	184	-10.7	Blue	136
J0931+2632	53269	142.817	26.550	0.0458	11.0	12.4	345	-12.6	Red	258
J0936+3204	33214	144.101	32.079	0.0269	10.3	11.8	217	-11.7	Red	158
J0937+1658	55745	144.292	16.977	0.0278	10.9	12.0	263	-10.3	Blue	192
J0951+3537	22822	147.937	35.622	0.0270	10.6	11.7	197	-10.4	Blue	143
J0958+3204	33737	149.714	32.073	0.0270	10.7	12.1	272	-12.7	Red	198
J1002+3238	33777	150.711	32.645	0.0477	10.1	11.7	191	-11.9	Red	143
J1013+0501	8634	153.352	5.025	0.0464	10.1	11.4	153	-10.8	Blue	115
J1032+2112	55541	158.196	21.216	0.0429	10.6	11.7	202	-10.1	Blue	150
J1051+1245	23419	162.827	12.757	0.0400	10.4	11.5	175	-10.0	Blue	130
J1059+0517	9109	164.811	5.292	0.0353	11.1	12.6	387	-11.9	Red	284
J1100+1210	23457	165.048	12.171	0.0354	10.1	11.4	154	-10.7	Blue	114
J1100+1043	23477	165.200	10.728	0.0360	11.1	12.3	313	-11.0	Blue	231
J1115+0241	5701	168.789	2.699	0.0442	10.7	11.8	218	-10.9	Blue	162
J1120+0410	12452	170.026	4.177	0.0492	10.8	12.2	296	-12.1	Red	222
J1122+0314	5872	170.642	3.244	0.0446	10.5	11.9	239	-12.0	Red	178
J1127+2657	48604	171.943	26.960	0.0334	10.6	11.7	201	-11.0	Blue	147
J1131+1553	29898	172.954	15.897	0.0364	10.2	11.7	199	-12.0	Red	147
J1132+1329	29871	173.052	13.492	0.0342	10.2	11.4	158	-9.7	Blue	116
J1142+3013	48994	175.575	30.230	0.0322	10.7	11.8	222	-10.4	Blue	163
J1155+2921	49433	178.903	29.351	0.0458	10.5	11.6	180	-10.3	Blue	135
J1241+2847	50550	190.367	28.791	0.0350	10.3	11.5	166	-10.0	Blue	123
J1251+0551	13074	192.894	5.864	0.0486	10.9	12.0	242	-10.4	Blue	182
J1305+0359	13159	196.356	3.992	0.0437	10.4	11.5	172	-10.8	Blue	128
J1315+1525	26936	198.855	15.423	0.0266	10.7	12.1	283	-12.3	Red	206
J1317+2629	51025	199.440	26.486	0.0450	10.3	11.4	162	-10.4	Blue	121
J1325+2714	51161	201.345	27.249	0.0345	10.1	11.4	156	-9.8	Blue	115
J1348+2453	38018	207.142	24.891	0.0297	10.1	11.3	153	-10.5	Blue	112
J1354+2433	44856	208.546	24.556	0.0286	10.1	11.6	191	-11.8	Red	139
J1404+3357	31172	211.122	33.953	0.0264	10.3	11.8	211	-12.3	Red	154
J1406+0154	7121	211.678	1.915	0.0472	10.2	11.7	202	-11.8	Red	152
J1427+2629	45940	216.954	26.484	0.0325	10.4	11.9	225	-12.0	Red	165
J1430+0323	9615	217.508	3.398	0.0333	10.2	11.7	197	-11.1	Red	145
J1431+2440	38198	217.894	24.682	0.0378	10.7	12.1	261	-12.7	Red	193
J1454+3050	42191	223.516	30.846	0.0320	10.1	11.4	155	-9.8	Blue	114
J1502+0649	41743	225.517	6.823	0.0462	10.5	11.6	180	-10.2	Blue	135
J1509+0704	41869	227.340	7.078	0.0414	10.1	11.4	155	-9.6	Blue	115
J1515+0701	42025	228.781	7.021	0.0367	10.9	12.3	314	-11.9	Red	231
J1541+2813	28365	235.344	28.230	0.0321	10.4	11.5	173	-9.6	Blue	127
J1544+2740	28317	236.034	27.673	0.0316	10.1	11.6	191	-12.1	Red	140

^a Details on the COS-Halos survey can be found in the published work by Tumlinson et al. (2013); Werk et al. (2013).

^b Using prescription from Kravtsov et al. (2014).

^c Using prescription from Liang & Chen (2014).

^d Galaxies with sSFR > 10⁻¹¹ yr⁻¹ are defined as blue galaxies. Galaxies below this value are defined as red galaxies.

^e Escape velocity at the virial radii probed by the QSO sightline assuming a NFW profile for the galaxy's dark matter distribution.

TABLE 2
DESCRIPTION OF QSO SIGHTLINES AND ABSORPTION LINE MEASUREMENTS
FOR THE COS-GASS SURVEY.

QSO	RA _{QSO}	Dec _{QSO}	z _{QSO}	ρ (kpc)	ρ/R_{vir}	Θ^{a}	$W_{\text{Ly}\alpha}^{\text{b}}$ (Å)	$\Delta V_{\text{Ly}\alpha}^{\text{c}}$ (km s ⁻¹)	$v_{\text{Ly}\alpha}^{\text{d}}$ (km s ⁻¹)	$b_{\text{Ly}\alpha}^{\text{d}}$ (km s ⁻¹)	$W_{\text{SiIII}1206}$ (Å)	$\Delta V_{\text{SiIII}1205}^{\text{c}}$ (km s ⁻¹)	$v_{\text{SiIII}}^{\text{d}}$ (km s ⁻¹)	$b_{\text{SiIII}}^{\text{d}}$
J0159+1345	29.971	13.765	0.504	102	0.7	64	1.501±0.023	-150 – 380	93,358	85,14	–	–	–	–
J0808+0514	122.162	5.244	0.361	215	0.7	7	–	–	–	–	<0.050	–	–	–
J0852+0313	133.247	3.222	0.297	178	1.1	67	0.113±0.015	0 – 110	50	49	<0.051	–	–	–
J0909+3236	137.276	32.608	0.809	170	0.7	21	0.090±0.014	50 – 200	101	71	<0.041	–	–	–
J0914+0837	138.632	8.629	0.649	189	1.3	69	0.104±0.020	-50 – 80	30	45	<0.065	–	–	–
J0930+2848	142.508	28.816	0.487	214	1.2	42	<0.126	–	–	–	<0.108	–	–	–
J0931+2628	142.820	26.480	0.778	226	0.7	77	0.114±0.013	150 – 250	200	55	<0.043	–	–	–
J0936+3207	144.016	32.119	1.150	160	0.7	0 ^e	<0.113	–	–	–	<0.086	–	–	–
J0937+1700	144.279	17.006	0.506	63	0.2	64	0.135±0.021	-300 – -150	-204	67	<0.056	–	–	–
J0951+3542	147.850	35.714	0.398	226	1.1	3	0.839±0.014	-90 – 200	64	59	–	–	–	–
J0959+3203	149.812	32.066	0.564	162	0.6	0 ^e	0.420±0.016	-320 – -100	-238,-144	33,19	0.060±0.013	-300 – -200	-256	12
J1002+3240	150.727	32.678	0.829	119	0.6	40	<0.063	–	–	–	<0.062	–	–	–
J1013+0500	153.325	5.009	0.266	102	0.7	0 ^e	0.445±0.024	-180 – 50	-72	49	0.088±0.020	-120 – 0	-70	20
J1033+2112	158.270	21.204	0.315	214	1.1	45	0.437±0.033	-100 – 95	-1	50	<0.065	–	–	–
J1051+1247	162.857	12.796	1.281	140	0.8	73	0.781±0.022	-180 – 140	-37	75	–	–	–	–
J1059+0519	164.795	5.327	0.754	95	0.2	30	0.270±0.022	-100 – 100	6	44	<0.062	–	–	–
J1059+1211	164.984	12.198	0.993	171	1.1	61	0.225±0.014	-150 – 0	-61	26	<0.045	–	–	–
J1100+1046	165.199	10.770	0.422	108	0.3	0 ^e	–	–	–	–	–	–	–	–
J1115+0237	168.782	2.633	0.567	209	1.0	83	0.195±0.020	-100 – 100	2	37	0.065±0.012	-20 – 30	4	20
J1120+0413	170.021	4.223	0.545	162	0.5	78	0.830±0.018	50 – 390	201,370	73,21	0.172±0.015	150 – 290	194	26
J1122+0318	170.601	3.301	0.475	221	0.9	0 ^e	0.110±0.018	0 – 150	67	58	–	–	–	–
J1127+2654	171.902	26.914	0.379	140	0.7	26	0.705±0.021	-250 – 100	-28,-178	54,30	0.051±0.017	-80 – 20	-34	12
J1131+1556	172.905	15.946	0.183	176	0.9	0 ^e	–	–	–	–	–	–	–	–
J1132+1335	173.044	13.586	0.201	230	1.5	5	0.319±0.017	-40 – 130	57	55	<0.043	–	–	–
J1142+3016	175.551	30.270	0.481	104	0.5	50	0.886±0.023	-200 – 170	3	67	0.227±0.019	-150 – 50	-33	53
J1155+2922	178.970	29.377	0.520	208	1.2	1	0.742±0.023	-200 – 230	72,-150	60,13	0.056±0.015	40 – 160	92	66
J1241+2852	190.374	28.870	0.589	198	1.2	40	0.211±0.020	-120 – 170	33	95	<0.040	–	–	–
J1251+0554	192.853	5.906	1.377	200	0.8	57	0.409±0.021	-20 – 180	80	51	<0.063	–	–	–
J1305+0357	196.351	3.959	0.545	103	0.6	11	0.821±0.016	-160 – 180	67,-43	48,59	–	–	–	–
J1315+1525	198.938	15.432	0.448	155	0.5	17	0.405±0.018	-50 – 170	64	48	0.131±0.017	0 – 150	49	48
J1318+2628	199.508	26.475	1.234	198	1.2	86	0.184±0.032	-120 – 120	0	50	–	–	–	–
J1325+2717	201.266	27.289	0.522	199	1.3	55	–	–	–	–	<0.095	–	–	–
J1348+2456	207.093	24.947	0.293	153	1.0	81	0.474±0.035	-230 – 0	-97	76	<0.073	–	–	–
J1354+2430	208.604	24.502	1.878	155	0.8	78	0.545±0.034	-170 – 50	-97,-5	37,26	<0.084	–	–	–
J1404+3353	211.118	33.895	0.549	111	0.5	57	0.749±0.027	-150 – 150	-26	75	0.177±0.024	0 – 150	37	45
J1406+0157	211.732	1.954	0.427	222	1.1	67	–	–	–	–	<0.061	–	–	–
J1427+2632	216.898	26.537	0.364	170	0.8	0 ^e	–	–	–	–	<0.078	–	–	–
J1429+0321	217.420	3.357	0.253	231	1.2	0 ^e	0.807±0.027	-150 – 250	-39,109	68,104	0.052±0.017	-50 – 50	-21	42
J1431+2442	217.858	24.706	0.407	110	0.4	18	0.569±0.015	0 – 220	73,156	40,28	<0.048	–	–	–
J1454+3046	223.601	30.783	0.465	223	1.4	37	0.472±0.035	-50 – 160	57	47	<0.079	–	–	–
J1502+0645	225.517	6.754	0.288	224	1.2	80	0.438±0.013	-150 – 110	12,-55	38,72	<0.032	–	–	–
J1509+0702	227.368	7.043	0.418	130	0.8	62	0.956±0.022	-275 – 130	49,-18,-215	29,84,30	0.137±0.011	-275 – -195	-239	21
J1515+0657	228.781	6.952	0.268	180	0.6	14	0.270±0.023	-500 – -300	-367	43	<0.061	–	–	–
J1541+2817	235.340	28.285	0.376	128	0.7	0 ^e	0.864±0.011	-520 – -250	-363	90	<0.039	–	–	–
J1544+2743	236.114	27.723	0.163	196	1.0	55	0.191±0.022	50 – 210	126	69	<0.064	–	–	–

^a Orientation of the QSO sightlines with respect to the disk of the galaxies. The values are based on SDSS r-band photometric measurements.

^b Limiting equivalent width denotes 3σ uncertainty.

^c Full width of the absorption feature in the rest-frame of the galaxy.

^d Centroid and b-value of the multiple components of the Lyman α and Si III absorption feature as estimated via Voigt profile fit. These are printed in the order of the strength of the component.

Redshift of the absorber $z_{\text{abs}} = z_{\text{gal}} + v_{\text{transition}}/c$, where z_{gal} is the systemic redshift of the galaxy (from Table 1) and c is the speed of light in vacuum.

^e Face-on galaxies.

